Journal of the Meteorological Society of Japan

The DOI for this manuscript is
DOI:10.2151/jmsj.2023-023
J-STAGE Advance published date: June 1st, 2023

Effects of Storm Size on the Interactions between Mid-Latitude Westerlies and Tropical Cyclones during Extratropical Transition in the Western North Pacific

Nao TAKAMURA [1]

Atmosphere and Ocean Department, Japan Meteorological Agency, Tokyo, Japan

Akiyoshi WADA, Wataru YANASE

Department of Typhoon and Severe Weather Research, Meteorological Research Institute, Tsukuba, Japan

and

Yoshiaki MIYAMOTO

Faculty of Environment and Information Studies, Keio University, Kanagawa, Japan
RIKEN Center for Computational Science, Kobe, Japan

July 8, 2022
Revised May 16, 2023

----

1) Corresponding author: Nao Takamura, Atmosphere and Ocean Department, Japan Meteorological Agency, 3-6-9 Toranomon, Minato-ku, Tokyo 105-8431, JAPAN
Email: n_takamura@met.kishou.go.jp
Tel: +81-3-6758-3900

Abstract

In 2019, serious disasters were caused by local strong winds associated with Typhoon Faxai and wide torrential rains with Typhoon Hagibis. Although both tropical cyclones (TCs) moved similar tracks and underwent extratropical transition after the recurvature (ETR), they had different sizes and structures: Faxai was a small axisymmetric TC, whereas Hagibis was a large asymmetric TC. The purpose of this study is to elucidate the effect of storm size on a TC that undergoes ET and its associated synoptic environment. Hagibis causes a larger amount of precipitation more widely than Faxai. The large amount of diabatic heating closely associated with the precipitation leads to low potential vorticity (PV) production downstream of Hagibis in the upper troposphere and the enhancement of the ridge. In contrast, the diabatic heating is relatively small and the production of low PV area is indistinct downstream of Faxai. In addition to the case studies, large (LA) and small (SM) TCs that undergo ETR (LA-ETR and SM-ETR TCs, respectively) in the western North Pacific over 2016-2020 are statistically compared based on cyclone phase space and composite analyses using the best track and Japanese 55-year Reanalysis datasets. As observed in the case studies, the LA-ETR TCs are characterized by a larger amount of precipitation and enhancement of downstream ridge compared to the SM-ETR TCs. The LA-ETR TCs change into asymmetric structures more drastically than the SM-ETR TCs while they move northward along the westerly jet with increasing the amplitude of the north-south meander. In contrast, the amplitude of the north-south meander of the westerly jet does not increase around the SM-ETR TCs. Therefore, the larger the storm size is, the larger the amplitude of the north-south meander of the westerly jet is, which results in the more drastic asymmetric structural change of the TC.

Keywords extratropical transition; cyclone phase space; structural change; westerly jet

1. Introduction

Extratropical transition (ET) is the process that is associated with the transformation of a tropical cyclone (TC) into an extratropical cyclone in a baroclinic environment and the reduction in sea surface temperature (SST) at high latitudes (Evans et al. 2017). A cyclone frequently produces intense rains and strong winds during ET, which results in a serious threat to land and maritime activities (Jones et al. 2003). During the 2019 typhoon season in the western North Pacific (WNP), Typhoons Faxai (the 15th TC in 2019, hereafter T1915) and Hagibis (the 19th TC in 2019, hereafter T1919) caused severe disasters during their passage over the Japanese archipelago. Both TCs made landfall in Japan, underwent ET over the ocean east of Japan while following similar tracks (Fig. 1). The maximum sustained surface wind speeds of both TCs at landfall were 40 m s^{-1} (Japan Meteorological Agency (JMA) 2019a). T1915 was small but it brought record-breaking strong winds and caused serious disasters in the east of Tokyo (cf. the location of Tokyo is indicated by the star symbol in Fig. 1b) around the landfall time (JMA 2020a). In contrast, T1919 was large and had already brought heavy rains to the Japanese archipelago before making landfall. Continuation of the heavy rains for several days caused river flooding over a wide area, particularly on the eastern side of the Japanese archipelago (JMA 2019b).

The two TCs were intensively examined because of the severe disasters they caused. A numerical simulation of T1915 reproduced observed features such as the small size of its vortex and its axisymmetric structure (Miyamoto et al. 2022). Miyamoto et al. (2022) pointed out that the environmental conditions such as high SST, large surface heat flux, and small vertical wind shear were favorable for the development of T1915. Regarding T1919, Yanase et al. (2022) demonstrated the influences of the westerly jet stream and the baroclinic zone on the asymmetric structure of T1919 during ET. One of the remarkable environmental characteristics of T1919 was the positive SST anomaly in WNP (Ito and Ichikawa 2021). Ito and Ichikawa (2021) indicated that warm SST accelerated T1919 near the Japanese archipelago, since the TC became embedded in the mid-latitude westerly jet earlier than a typical TC. The warm SST anomaly had a potential to shift the low-level front inland and acted to increase precipitation caused by T1919 along the Pacific coast of northeastern Japan (Iizuka et al. 2021). The record-breaking heavy rainfalls caused by T1919 were attributed to moist absolute instability, abundant moisture and high humidity (Takemi and Unuma 2020). The upper ocean heat content from the surface to the depth of the 26 °C isotherm underneath both T1915 and T1919 was higher than the climatological mean (Wada and Chan 2021). Apart from the increases in SST and upper ocean heat content in 2019, historical atmospheric and oceanic warming intensified T1919 and helped enhance the associated extremely heavy precipitation (Kawase et al. 2021).

These studies on T1915 and T1919 revealed the characteristics of these TCs and their surrounding environments. Some features of the two TCs including their recurved tracks, landfalls in Japan and ET east of Japan were similar, but their structures and storm sizes differed: T1915 was a small axisymmetric TC, whereas T1919 was a large asymmetric

TC. The differences in the symmetry of TC structure are expected to be due to [1] differences in the stages during ET in which the structure changes from symmetric to asymmetric and/or [2] differences in the effect of storm size on the ET process. However, few studies examined the impacts of storm size on ET. In addition, there is a question of whether the differences such as observed between T1915 and T1919 are specific to events or are caused by systematic physical mechanisms. This issue may be solved by statistical approaches. Takamura and Wada (2020) used a statistical approach to investigate TCs which underwent ET in August and September 2016. They concluded that the unusual characteristics of ET during August 2016, such as the frequent ET and indistinct structural changes from a warm-core to a cold-core, could be explained by the synoptic environments such as enhanced undulation of the mid-latitude upper-tropospheric jet stream.

The downstream development during ET has been already examined by previous studies. Keller et al. (2019) discussed “direct impacts” and “downstream impacts” of ET on the mid-latitude flow. The direct impact of ET was characterized by an enhanced ridge building immediately downstream of a transitioning cyclone and a development of a jet streak, which crucially depended on the phasing between the transitioning cyclone and the developing or already-existing mid-latitude wave pattern. Riboldi et al. (2019) highlighted the following two contributions to downstream impacts of ET. One was a “diabatic” contribution of the irrotational outflow and the other was an “adiabatic” contribution based on the interplay between an upper-level potential vorticity (PV) anomaly (trough) and a lower-level potential temperature anomaly. A negative PV advection by diabatic outflow initiated ridge building, and accelerated a mid-latitude, upper-level jet streak (Grams 2011, Grams et al. 2013, Quinting and Jones 2016, Grams and Archambault 2016). As for an “adiabatic” contribution, the interaction of a TC with a mid-latitude trough strongly modulated the extent and intensity of the precipitation (Atallah and Bosart 2003). A mid-latitude flow amplification to recurving TCs was governed by the characteristics of large-scale flow (Archambault 2011, Riboldi et al. 2018, Finocchio and Doyle 2019). The development of amplified extratropical flow following the passage of a recurving TC was shown to be sensitive to the strength of the TC–extratropical flow interaction (Archambault et al. 2013, 2015).

The purpose of this study is to reveal whether the differences in the symmetry of TC structure as observed between T1915 and T1919 are associated with [1] differences in the stages during ET or [2] differences in the effect of storm size on the ET process. To statistically elucidate these effects on the differences in the symmetry of TC structure, we investigate TCs from 2016 to 2020 in addition to case studies for T1915 and T1919. The rest of this paper is organized as follows. Section 2 describes datasets used in this study and explains a method used to classify TCs from 2016 to 2020. Characteristics are compared between each type classified based on this method in Section 3. We investigate the symmetry, the cold-core or warm-core features of the TCs, and the synoptic environments surrounding the TCs such as lower-tropospheric baroclinicity. Moreover, the relationship between the storm size and the mid-latitude westerly jet is identified through the combination of the statistical approaches and case studies. Section 4 discusses the TCs and their associated winds and precipitation, and the conclusions of this study are summarized in Section 5.

2. Data and methods

2.1 Data and determination of ET

We investigate the characteristics of WNP TCs such as latitude and longitude, central pressure, 10-minute mean maximum sustained wind speed, and radii of 25 m s^{-1} and 15 m s^{-1} winds using the best track data archived in the Regional Specialized Meteorological Center (RSMC) Tokyo (JMA 2020b). In addition, the radius of maximum wind (RMW) recorded in the Joint Typhoon Warning Center (JTWC) best track data (JTWC 2022) is used to investigate RMW. Individual TCs are given an alphanumeric name (TC number) that includes the last two digits of the year and the 2-digit serial number of a TC in that year such as T1915 and T1919 (Table 1). The 6-hourly Japanese 55-year Reanalysis (JRA-55, Kobayashi et al. 2015) product with a horizontal resolution of 1.25° × 1.25° is used for determining ET based on a cyclone phase space (CPS, Hart 2003) analysis. The CPS is composed of three cyclone parameters (B, $-V_T^L$ and $-V_T^U$) calculated using isobaric geopotential height (Z). The parameter B is a metric of an asymmetry of the TC-motion-relative thickness:

$$B = h\left[\left(\overline{Z_{600hPa} - Z_{900hPa}}\right)_R - \left(\overline{Z_{600hPa} - Z_{900hPa}}\right)_L\right],$$

where the subscript *R* (*L*) indicates right (left) relative to the TC motion, and the overbar indicates the areal mean over a semicircle of radius 500 km. The integer *h* takes a value of +1 for the Northern Hemisphere and -1 for the Southern Hemisphere. The parameter $-V_T^L$ ($-V_T^U$) is a metric of the thermal wind relationship in the lower (upper) layer that assesses a cold-core or warm-core structure of the TC:

$$-V_T^L = \frac{\delta(\Delta Z)}{\delta lnp}\Big|_{900hPa}^{600hPa} \text{ and}$$

$$-V_T^U = \frac{\delta(\Delta Z)}{\delta lnp}\Big|_{600hPa}^{300hPa},$$

where ΔZ is a geopotential perturbation calculated by $Z_{max} - Z_{min}$ and Z_{max} (Z_{min}) is the maximum (minimum) value evaluated within a radius of 500km. Each parameter is calculated by using data with a horizontal resolution of 0.25° linearly interpolated from the JRA-55 data with a coarse horizontal resolution of 1.25°. The onset and completion of ET are determined by the following criteria (Evans and Hart 2003, Takamura and Wada 2020):

- Onset of ET (hereafter TB): the time when the value of *B* exceeds 10 m and
- Completion of ET (hereafter TE): the time when the value of $-V_T^L$ becomes negative.

We regard the following TCs as ET cases: TCs that meet the TE criterion (transforming into a cold-core structure) after meeting the TB criterion (transforming into an asymmetric structure) or TCs that simultaneously meet the TB and TE criteria. In other words, TCs that meet the TE criterion prior to meeting the TB criterion are excluded. The JRA-55 dataset is also used for analyzing the synoptic environments around the TCs that undergo ET. A lower-tropospheric baroclinicity and upper-tropospheric westerly jet (wind speed exceeding 20 m s^{-1}) are identified by using the JRA-55 isobaric level data. A PV is obtained from the JRA-55 isentropic level data. We examine precipitable water as a potential measure of diabatic heating caused by TCs using the JRA-55 total column data. A 24-hour accumulated precipitation is calculated by using the hourly global precipitation dataset obtained from the Global Satellite Mapping of Precipitation (GSMaP) version 7 by Japan Aerospace Exploration Agency (JAXA) (Kubota et al. 2020). The period covered by this dataset begins in 2016. The 24-hour accumulated precipitation is defined by the total hourly precipitation during the previous 24 hours.

2.2 Classification of TCs

We analyze WNP TCs for five years from 2016 to 2020 since the GSMaP product is available from 2016. Note that this period includes August 2016 when the enhanced undulation of the upper-tropospheric jet stream affected ET events (Takamura and Wada 2020). Out of a total of 134 TCs from 2016 to 2020, 48 TCs (35.8%) undergo ET, and the remaining 86 TCs weaken into tropical depressions without undergoing ET (hereafter no-ET). Figure 2 shows the time series of CPS parameters ($-V_T^L$, $-V_T^U$, and B) from 36 hours before TB (TB - 36) to 36 hours after TE (TE + 36) for T1915 and T1919. According to the CPS analysis, T1919 becomes an asymmetric structure and meets the TB criterion (B > 10 m), and then has a cold-core structure and meets the TE criterion ($-V_T^L$ < 0: dashed red lines in Fig. 2a and 2c). Then, the asymmetric structure become more prominent. In contrast, T1915 has a relatively small asymmetric structural change after undergoing TB compared with T1919 (dashed blue lines in Fig. 2a and 2c). The difference in the asymmetric structural change associated with ET between the two TCs therefore could not be explained by only the difference in the stages during ET.

We then investigate the difference in the effect of storm size on the ET process. We classify the WNP TCs as follows. First, the largest radius of 25 m s^{-1} (R25) and 15 m s^{-1} (R15) winds are examined for 134 TCs from 2016 to 2020 archived in the RSMC-Tokyo best track data. The maximum values of R25 and R15 during the life cycle of an individual TC are defined as Max_R25 and Max_R15, respectively. The mean Max_R25 and Max_R15 are 149.6 km and 438.6 km for the 134 TCs, respectively. Separating the 134 TCs into the ET and no-ET cases, the mean Max_R25 and Max_R15 are 182.1 km and 518.9 km for the ET cases, respectively, and 116.5 km and 395.2 km for the no-ET cases, respectively. Because most of the TCs have Max_R25 and Max_R15 before TB, the difference in the storm size between ET and no-ET cases is unlikely to result from an expansion of the storm size associated with TCs that undergo ET. The TCs are classified based on the following criteria for Max_R25 and Max_R15 that are determined subjectively (Fig. 3). The TCs without Max_R25 are classified based on only Max_R15.

・Large TCs：Max_R25 ≧ 120 nm (～222.2 km) and Max_R15 ≧ 350 nm (～648.2 km),

・Small TCs：Max_R25 < 70 nm (～129.6 km) and Max_R15 < 200 nm (～370.4 km).

Hereafter, large TCs are referred to as LA, small TCs as SM and the rest (middle TCs) as MID although MID TCs will not be deeply investigated in this study. After that, we extract the ET cases from each type based on the CPS diagnosis (Section 2.1). The SM TCs are further classified into TCs that undergo ET without the recurvature, which occurs over the South China Sea (dashed lines in Fig. 1b referred to as SM-SCS), and the other TCs that undergo ET after the recurvature (solid lines in Fig. 1b; referred to as SM-ETR). In the SM-SCS TCs, even though the CPS-based diagnosis suggests ET, the characteristics can be different from the SM-ETR TCs. This is because the right and left sides relative to the direction of TC motion used in the calculation of parameter B, which correspond to the north and south sides, are different between the SM-SCS and SM-ETR TCs. The analyzed LA TCs that undergo ET are associated with the recurvature (referred to as LA-ETR). The differences in the characteristics between LA-ETR and SM-ETR TCs are evaluated at the 95% significance level based on a two-sided Student's *t*-test (Section 3.1 and 4).

3. Results

3.1 Characteristics of LA-ETR and SM-ETR TCs

Based on the criteria described in Section 2.2, the number of LA and SM TCs are 15 (11.2%) and 47 (35.1%), respectively, out of the total number of 134 TCs from 2016 to 2020 (Fig. 4a). Among the 48 ET cases (35.8% to the total TCs), the number of LA TCs is 10 (20.8%) and that of SM TCs is 11 (22.9%) (Fig. 4b). Among the 86 no-ET cases, the number of LA TCs is 5 (5.8%) and that of SM TCs is 36 (41.9%) (not shown). These results indicate that the number of LA and SM TCs are almost equivalent for the ET cases, while the number of SM TCs are more than that of LA TCs for the no-ET cases. LA TCs occur only from July to October, whereas SM TCs occur throughout the year (Fig. 5b). The ratio of SM TCs to the total number of TCs is higher than that of LA TCs from July to September (Fig. 5b), when TCs frequently occur (Fig. 5a). The ratio of LA TCs to the total number of TCs increases from September to October (Fig. 5b), when ET frequently occurs (Fig. 5a), and is comparable with that of SM TCs in October (Fig. 5b). LA TCs tend to be less frequent in years when ET rarely occurs, and more frequent in years when ET frequently occurs (Supplement 1). These results suggest that LA TCs are more likely to undergo ET than SM TCs.

In the following paragraphs, we focus on the ET cases. Among the ET cases, the number of LA-ETR TCs is 10, that of SM-ETR TCs is 6 and that of SM-SCS TCs is 5 (Table 1). Hereafter, we will compare the LA-ETR TCs with the SM-ETR TCs. Figure 1 shows the tracks, and the positions at the time of the maximum intensity during the life cycle of a TC (hereafter TM), TB and TE for the LA-ETR and SM-ETR TCs. It should be noted that the maximum intensity is determined based on the minimum central pressure. Most of the LA-ETR TCs recurve south of Japan and then undergo TB (Fig. 1a). After TB, they approach Japan, make landfall and undergo TE. The SM-ETR TCs recurve and undergo TE south of Japan, rarely make landfall in Japan (solid lines in Fig. 1b).

Table 2 compares the characteristics of the LA-ETR and SM-ETR TCs listed in Table 1. The mean latitude at TE for the LA-ETR TCs is 41.2°N and that for the SM-ETR TCs is 31.6°N, which is significantly different at the 95% significance level based on the *t*-test. The LA-ETR TCs thus tend to undergo TE at higher latitude than the SM-ETR TCs. On the other hand, the mean latitude at TM for the LA-ETR TCs is 23.2°N and that for the SM-ETR TCs is 25.4°N, and that at TB for the LA-ETR TCs is 34.0°N and that for the SM-ETR TCs is 31.0°N, these differences are not significant at the 95% significance level based on the *t*-test. Kitabatake (2011) reported that the monthly mean latitude of ET varies from 25°N in winter to the north of 40°N in August. We therefore compare the position at TE between the LA-ETR and SM-ETR TCs by month in order to consider the seasonal variation of the ET characteristics (not shown). Although the number of TCs for each month is small and their positions vary from case to case, the LA-ETR TCs tend to undergo TE at higher latitude than the SM-ETR TCs. These results suggest that the latitude of TE differs between the LA-ETR and SM-ETR TCs, which is independent of the seasonal variation.

The mean duration of TCs from TM to TB and that from TB to TE are longer for the LA-ETR TCs (73.2 hours and 22.8 hours, respectively) than for the SM-ETR TCs (26.0 hours and 3.0 hours, respectively), which is significantly different at the 95% significance level based on the *t*-test. In this study, the moving speed of a TC is estimated from the east-west and north-south distances that the TC moves during the previous 6 hours (hereafter U_{move} and V_{move}, respectively). Note that for the cases including data for shorter time intervals in the RSMC-Tokyo best track data, the data is also used. The mean V_{move} before TB (from TM to TB) is 6.2 m s^{-1} for both the LA-ETR and SM-ETR TCs, and that after TB (from TB to the time of the final record in the RSMC-Tokyo best track data) is 9.3 m s^{-1} for the LA-ETR TCs and 5.4 m s^{-1} for the SM-ETR TCs. The difference in V_{move} after TB is significant at the 95% significance level based on the *t*-test. The LA-ETR TCs therefore tend to move northward with relatively fast moving speeds compared with the SM-ETR TCs. Comparing U_{move} between LA-ETR and SM-ETR TCs, the LA-ETR TCs tend to move westward before TB, whereas the SM-ETR TCs tend to move eastward, which is significantly different at the 95% significance level based on the *t*-test. On the other hand, both the LA-ETR and SM-ETR TCs tend to move eastward after TB although the moving speeds for the SM-ETR TCs is slightly faster than those for the LA-ETR TCs. These results suggest that although the SM-ETR TCs tend to move relatively eastward, the difference in the moving speeds between LA-ETR and SM-ETR TCs is mainly due to the difference in poleward moving speeds for the LA-ETR TCs.

The CPS analysis is then conducted for the LA-ETR and SM-ETR TCs to investigate the differences in the structural change between them. Figure 2 shows the time series of CPS parameters ($-V_T^L$, $-V_T^U$, and B) from 36 hours before TB (TB – 36) to 36 hours after TE (TE + 36). The data is composited for the LA-ETR and SM-ETR TCs on the basis of time relative to TB and TE (cf. Table 1). The data from TB to TE is composited on the basis of time relative to TB, and the number of data samples differs because this duration for an individual TC is different. In Fig. 2, the data is plotted only when there are three or more TCs at a time slot (Fig. 2d). The parameters $-V_T^L$ (Fig. 2a) and $-V_T^U$ (Fig. 2b) are positive (warm-core structure) and greater for the LA-ETR TCs than for the SM-ETR TCs before TB. The presence of deep, warm-core structures suggests that the LA-ETR TCs have typical TC structures. The difference could be associated with the relatively long duration from TB to TE for the LA-ETR TCs compared with the SM-ETR TCs (Table 2) because the transition from the robust warm-core structures to cold-core ones is expected to take time. It should be noted that the horizontal resolution of the JRA-55 dataset could be too coarse to adequately represent the warm-core structures of the SM-ETR TCs. The parameter *B* drastically changes after TB for the LA-ETR TCs (asymmetric structure), whereas the change of parameter *B* is relatively small for the SM-ETR TCs (Fig. 2c). The LA-ETR TCs therefore tend to drastically change into asymmetric structures, whereas the SM-ETR TCs tend to undergo relatively small asymmetric structural changes. In this analysis, the CPS parameters are calculated within the same radius of 500 km for all of the LA-ETR and SM-ETR TCs. We recalculate the CPS parameters within Max_R15 for individual TCs instead of a radius of 500 km to investigate the effect of storm size on the CPS parameters. The mean Max_R15 for the LA-ETR TCs is 759.3 km and that for the SM-ETR TCs is 287.1 km (Table 2). The absolute values of the parameter *B* for the LA-ETR TCs becomes larger for the calculation within Max_R15 than that within radius of 500 km, and the asymmetric structural changes are more distinct. In contrast, the absolute values of the parameter B for the SM-ETR TCs becomes smaller, and the asymmetric structural changes are more indistinct. Calculated CPS parameters for the individual storm size ensure the drastic changes into the asymmetric structures for the LA-ETR TCs compared with those for the SM-ETR TCs. However, it should be noted that this analysis cannot exactly separate the inner core structure of SM-ETR TC from the synoptic environment because of the relatively coarse horizontal resolution of the JRA-55 dataset.

Next, the synoptic environments during ET are investigated by comparing between the composite maps for the LA-ETR and SM-ETR TCs using the JRA-55 dataset to clarify the relationship between the storm size and the synoptic environments. The composited synoptic environments are produced around the center in each TC at TB and TE. We focus on the lower-tropospheric baroclinicity represented by the horizontal gradient of temperature at 850 hPa (Fig. 6). The baroclinic zone evidenced by a steep temperature gradient appears on the north side of the TC center for LA-ETR TCs (about 1000 km from the TC center) at TB (Fig. 6a), where relatively warm (cold) air is expected to be advected on the east (west) side of the TC center from the south (north). As the LA-ETR TCs approach the baroclinic zone at TE, the advection of warm and cold air becomes strong, and the temperature gradient near the TC center becomes steep (Fig. 6b). As for the SM-ETR TCs, the baroclinic zone also appears on the north side of the TC center at TB (Fig. 6c). However, the baroclinic zone remains far from the TC center even at TE (about 1000 km), and the advection of warm and cold air remains weak (Fig. 6d). Therefore, the strengthening of the advection of warm air from the south and cold air from the north around the LA-ETR TCs is expected to increase their lower-tropospheric baroclinicity, and the LA-ETR TCs drastically change into the asymmetric structures. In contrast, since the advection of warm and cold air around the SM-ETR TCs is indistinct, their lower-tropospheric baroclinicity remains weak and the asymmetric structural changes are relatively small.

3.2 Relationship between the storm size and the westerly jet

In this section, we identify the relationship between the storm size and the westerly jet. Figure 7 compares the composited distributions of horizontal wind at 300 hPa for the LA-ETR and SM-ETR TCs produced in a similar manner to Fig. 6. The amplitude of the north-south meander of the westerly jet is larger for the LA-ETR TCs (Fig. 7a). As the LA-ETR TCs approach the westerly jet, the ridge is enhanced downstream of the TCs, and the amplitude of the north-south meander of the westerly jet increases (Fig. 7b). In addition, the wind speed in the westerly jet increases. The TCs move northeastward along the westerly jet with the increasing amplitude of the north-south meander (see also Fig. 1a). The distribution of horizontal flow at TE resembles a “double jet pattern” which is frequently found when extratropical cyclones rapidly develop, in which a TC center is located on the right side of the entrance of a northeastern jet streak and on the left side of the exit of a southwestern jet streak (Kitabatake 2019, blue circle in Fig. 7b). According to Kitabatake (2019), this position of TC center is in front of the trough, where upward motion could be induced due to divergence. For the SM-ETR TCs, the westerly jet is zonal with a strong wind speed, and the amplitude of the north-south meander is relatively small (Fig. 7c). The SM-ETR TCs move south of the westerly jet, the ridge downstream of the TCs remains weak, with little change in the wind speed in the westerly jet and the amplitude of the north-south meander (Fig. 7d).

We also use a PV to better understand the relationship between the storm size and the westerly jet. A PV (unit: PVU = 10^{-6} m^2 s^{-1} K kg^{-1}) is useful for understanding the variations in the westerly jet and the changes that accompany isentropic processes during those variations (Hoskins et al. 1985). To clearly describe the correspondence between the change in the amplitude of the north-south meander of the westerly jet and that of the PV distribution, we present the results of representative cases: T1919 for LA-ETR TCs and T1915 for SM-ETR TCs. T1919 undergoes TB at 0000 UTC on 12 October and TE at 0600 UTC on 13 October, and T1915 undergoes TB at 0600 UTC on 9 September and TE at 1200 UTC on 9 September according to the CPS analysis (Table 1). Figures 8 and 9 show the horizontal distributions of 355-K isentropic PV (a and c) in addition to 300-hPa horizontal wind (b and d) for T1919 and T1915, respectively. In the case of T1919, a westerly jet with a relatively large amplitude of its north-south meander is located north of the center of TC (Fig. 8b). A relatively high PV is distributed around the center of TC (white circle in Fig. 8a), and a relatively low PV is on its north side (35°–50°N, 140°–155°E in Fig. 8a). As T1919 moves northeastward, the low PV area on the north of the center of TC spreads northward and northeastward (45°–55°N, 155°–175°E in Fig. 8c), and the north-south gradient of PV increases. These changes correspond to an enhancement of the ridge downstream of the TC (Fig. 8d), which is expected to contribute to further increase in the amplitude of the north-south meander of the westerly jet. T1919 moves northeastward along the western edge of the ridge (Fig. 8d). In the case of T1915, a westerly jet is zonal with a smaller amplitude of the north-south meander north of the center of TC than in the case of T1919 (Fig. 9b). The northward spread of low PV area and the increase in the north-south gradient of PV found in the case of T1919 are indistinct in the case of T1915 (Figs. 9a and 9c). These characteristics correspond to a weak ridge and a small amplitude of the north-south meander of the westerly jet around the TC (Fig. 9d). In addition, the high PV area around the center of T1915 is not as large as that around the center of T1919 (Figs. 8a and 9a). Further investigations indicate that the relatively high PV area around the center of T1919 is found up to around 355-K isentropic level, whereas the high PV area around the center of T1915 is only below around 345-K isentropic level (not shown). The results indicate that the positive PV tower around the center of T1919 tends to be relatively tall compared with that around the center of T1915.

3.3 Effect of diabatic heating associated with the storm size

The PV distributions shown in Section 3.2 reveal that the ridge is enhanced and the amplitude of the north-south meander of the westerly jet increases around T1919, but the enhancement of the ridge and the increase in the amplitude of the north-south meander are indistinct downstream of T1915. Riblodi et al. (2019) highlighted the importance of irrotational outflow from diabatic processes in an enhancement of ridge (negative PV) building on the evolution of the mid-latitude flow. To investigate the difference of diabatic heating between T1919 and T1915, we examine 24-hour accumulated precipitation calculated using the GSMaP dataset. Figure 10 shows the horizontal distributions of 24-hour accumulated precipitation at TB and TE for T1919 and T1915. We define 24-hour accumulated precipitation as the total hourly precipitation during the previous 24 hours from TB or TE. The location of TC center is indicated by the black circle with the origin of black arrow showing the location 24 hours before. The precipitation is large and spreads widely downstream of T1919 (Figs. 10a and 10b). In contrast, the precipitation area is relatively small and concentrates around T1915 (Figs. 10c and 10d).

Since a clear difference of 24-hour accumulated precipitation that related to diabatic heating around the TC center is analyzed between T1919 and T1915, composite analyses are conducted again for LA-ETR and SM-ETR TCs listed in Table 1. To compare the difference of 24-hour accumulated precipitation distribution quantitatively, the 24-hour accumulated precipitation is area-integrated within Max_R15 for each TC, and then these values for each time during TB and TE are averaged. Averaging for each type, the mean 24-hour accumulated precipitation is 8.0×10^{13} kg for the LA-ETR TCs and larger than the corresponding precipitation of 1.2×10^{13} kg for the SM-ETR TCs. We also calculate the 24-

hour accumulated precipitation within the mean Max_R15 of the LA-ETR and SM-ETR TCs for all of the LA-ETR and SM-ETR TCs in order to investigate the effect of storm size on the precipitation. The mean Max_R15 for the LA-ETR TCs (large radius) is 410 nm (～759.3 km) and that for the SM-ETR TCs (small radius) is 155 nm (～287.1 km). The mean 24-hour accumulated precipitation within the large radius for the LA-ETR TCs is 7.9×10^{13} kg and that for the SM-ETR TCs is 4.4×10^{13} kg, that within the small radius for the LA-ETR TCs is 1.8×10^{13} kg and that for the SM-ETR TCs is 1.1×10^{13} kg. The mean difference of 24-hour accumulated precipitation between the large and small radii is large for the LA-ETR TCs (6.1×10^{13} kg) but small for the SM-ETR TCs (3.2×10^{13} kg). This difference suggests that the area of 24-hour accumulated precipitation is relatively wide around the center of LA-ETR TCs and concentrates around the center of SM-ETR TCs. This result of composite analysis is consistent with the result of case studies shown in Fig. 10.

In addition, we examine precipitable water as a potential measure of diabatic heating caused by TCs. The precipitable water (hereafter PWAT; kg) is area-integrated within Max_R15 for each TC using the total column data archived in the JRA-55 product (kg m^{-2}). Figure 11 compares the time series of mean PWAT for the LA-ETR and SM-ETR TCs. The LA-ETR TCs have a relatively large amount of PWAT compared with that of the SM-ETR TCs (lines in Fig. 11). When the PWAT is compared per unit area, the difference between LA-ETR and SM-ETR TCs is small (not shown). This difference suggests that the LA-ETR TCs have a larger amount of PWAT than the SM-ETR TCs due to their relatively large size, which indicates that the PWAT is related to the storm size. The PWAT decreases after TB for the LA-ETR TCs (red line in Fig. 11), whereas the decrease in PWAT is relatively small for the SM-ETR TCs (blue line in Fig. 11). As shown in the PV distributions near the TC center (Section 3.2), the LA-ETR TCs tend to be relatively tall compared with the SM-ETR TCs. The LA-ETR TCs thus could cause a larger amount of diabatic heating up to the westerly jet level.

Based on the above results, the relationship between LA-ETR or SM-ETR TCs and the westerly jet could be summarized as follows. The LA-ETR TC causes a relatively large amount of precipitation widely when the TC approaches the westerly jet. The relatively large amount of diabatic heating inferred by the precipitation produces a low PV area downstream of the TC in the upper troposphere and increases the amplitude of the north-south meander of the westerly jet. In addition, since the LA-ETR TC is relatively tall compared with the SM-ETR TC, the LA-ETR TC does affect the westerly jet level. The LA-ETR TC moves northward along the westerly jet with increasing the amplitude of the north-south meander. At that time, the LA-ETR TC drastically changes into an asymmetric structure. The LA-ETR TC is expected to interact with the westerly jet. In contrast, the SM-ETR TC causes a relatively small amount of precipitation. The amplitude of the north-south meander of the westerly jet remains weak because the amount of diabatic heating around the SM-ETR TC is relatively small and the production of low PV area in the upper troposphere is relatively indistinct compared with the LA-ETR TC. The SM-ETR TC moves south of the westerly jet and is far from the westerly jet, and the asymmetric structural change of the TC is small.

4. Discussion

The differences of ET between LA-ETR and SM-ETR TCs shown in the previous sections are expected to be also associated with the differences in the disasters caused by TCs. In this section, the relationship of LA-ETR or SM-ETR TCs with the minimum central pressure, maximum sustained wind speed, RMW and precipitation is discussed. First, the minimum central pressure and maximum sustained wind speed during the life cycle of the individual TC are examined by using the RSMC-Tokyo best track data. The mean minimum central pressure and mean maximum sustained wind speed are 939.0 hPa and 44.5 m s^{-1} for the LA-ETR TCs, respectively, and 967.5 hPa and 37.7 m s^{-1} for the SM-ETR TCs, respectively (Table 2). The difference of the minimum central pressure between LA-ETR and SM-ETR TCs is significant at the 95% significance level based on the *t*-test, but the difference in the maximum sustained wind speed is not significant. The pressure-wind relationship shows that the maximum sustained wind speeds tend to be stronger for the SM-ETR TCs than for the LA-ETR TCs at the same minimum central pressure (Fig. 12). The reason is considered that the SM-ETR TCs have relatively sharp radial pressure gradient due to the small size, whereas the radial pressure gradient around the center of LA-ETR TCs is relatively gradual due to the large size.

Next, we investigate RMW using the JTWC best track data. Figure 13 shows the

RMW at TM and that at TE for each TC. Since the number of data samples is different between the JTWC and RSMC-Tokyo best track data, the final record after TB of each TC is used as that at TE (during ET) for the cases without data at TE in the JTWC best track data. The RMW at TE is not considered for the cases without data after TB in the JTWC best track data. The RMW becomes larger at TE than at TM for most of the TCs, which is considered to be consistent with an expansion of strong wind area during ET (Evans and Hart 2008, Shin 2019). The RMW tends to be larger for the LA-ETR TCs than for the SM-ETR TCs at both TM and TE. The increase in RMW tends to be more distinct for the LA-ETR TCs than for the SM-ETR TCs. The mean RMW at TM for the LA-ETR TCs is 55.7 km and that for the SM-ETR TCs is 20.7 km, and that at TE for the LA-ETR TCs is 101.9 km and that for the SM-ETR TCs is 37.0 km (Table 2). The difference in RMW at TE between LA-ETR and SM-ETR TCs is significant at the 95% significance level based on the *t*-test, while the differences in RMW at TM and TB are not significant. Shin (2019) showed that the area of the local wind maximum and the cyclonic flow of a TC expanded because frontal convection (baroclinic zone) developed in the ET stage. These results suggest that the RMW increases due to the interactions between the LA-ETR TCs and the mid-latitude baroclinic zone whereas the RMW of the SM-ETR TCs does not increase as much as that of the LA-ETR TCs because the interactions rarely occur. Miyamoto et al. (2022) suggested that the small RMW of T1915 favored the strong intensity. The SM-ETR TCs such as T1915 have the small RMW and the winds associated with the TCs are strong around the TC center. In addition, the SM-ETR TCs tend to maintain typical symmetric TC structures due to few interactions with the westerly jet. The SM-ETR TCs could therefore cause relatively strong winds locally. On the other hand, the LA-ETR TCs cause a larger amount of precipitation more widely than the SM-ETR TCs (Section 3.3, Fig. 10). We therefore suppose that the LA-ETR TCs such as T1919 tend to be “rain-laden typhoons” that cause rain-related disasters, whereas the SM-ETR TCs such as T1915 are “typhoons with severe wind” that cause wind-related disasters. The more detailed study regarding the relationship between the storm size of TCs and the disasters caused by the TCs including the distributions of surface wind speed and precipitation is needed in the future.

Grams (2011) quantified the changes in the mid-latitude flow in five real ET cases including Typhoon Jangmi (2008) and revealed the diabatically enhanced net transport of low PV air from the lower troposphere to the jet level governing ridge building directly downstream of the ET system, lifting the tropopause and accelerating the upper-level jet streak. The joint interaction of the low-level TC circulation with the mid-latitude baroclinic zone as well as the upper-level TC outflow with the upper-level mid-latitude jet stream resulted in a net transport of low PV air to the jet level. The results of this study indicate that LA-ETR TCs can cause a relatively large amount of diabatic heating compared with SM-ETR TCs, which results in the low PV production downstream of the TCs in the upper troposphere and the increase in the amplitude of the north-south meander of the westerly jet. However, we do not address the effect of the advection of PV and the convection on ridge building. This should be quantitatively investigated in the future.

We compare the structural changes between LA-ETR and SM-ETR TCs using the JRA-55 dataset with a horizontal resolution of 1.25°. The size and structure of some SM-ETR TCs could not be fully resolved in the JRA-55 dataset because of its coarse horizontal resolution. An analysis using data with a horizontal resolution finer than the JRA-55 is the subject of a future study because we need to ensure the robustness of the results obtained in this study.

5. Conclusions

To elucidate the effect of storm size exemplified by the difference between T1915 and T1919 on a TC undergoes ET and its associated synoptic environment, we investigate WNP TCs from 2016 to 2020 by classifying into LA and SM types based on Max_R25 and Max_R15. We further focus on LA-ETR and SM-ETR TCs that undergo ET after the recurvature. The statistical comparisons by using the CPS and composite analyses are conducted between 10 LA-ETR and 6 SM-ETR TCs. In addition, the case studies examining the distributions of the 24-hour accumulated precipitation and PV for representative cases, T1919 for LA-ETR TCs and T1915 for SM-ETR TCs identify the relationship between the storm size and the westerly jet.

The schematic diagram on the interactions of TCs with a westerly jet with a focus on the differences between LA-ETR and SM-ETR TCs is shown in Fig. 14. The LA-ETR TCs cause a larger amount of precipitation more widely than the SM-ETR TCs. The relatively large amount of diabatic heating inferred by the 24-hour accumulated precipitation produces a low PV area on the northeast side (downstream) of the LA-ETR TCs in the upper troposphere. The low PV production leads to an enhancement of the ridge and increase in the amplitude of the north-south meander of the westerly jet. In addition, since a high PV associated with the LA-ETR TCs is distinct up to relatively high level compared with that associated with the SM-ETR TCs, diabatic heating for the LA-ETR TCs could affect the PV distribution up to the westerly jet level. The LA-ETR TCs drastically change into asymmetric structures while they move northward along the westerly jet with increasing the amplitude of the north-south meander. In contrast, the diabatic heating is relatively small and the production of low PV area is indistinct downstream of the SM-ETR TCs in the upper troposphere. The amplitude of the north-south meander of the westerly jet remains relatively small. The SM-ETR TCs tend to move south of the westerly jet and the asymmetric structural changes are relatively small compared with that of the LA-ETR TCs. The results suggest that the difference between LA-ETR and SM-ETR TCs can be explained by the fact that the LA-ETR TCs interact with the westerly jet whereas such interactions rarely occur for the SM-ETR TCs. The storm size affects the amplitude of the north-south meander of the westerly jet and then the amplitude of the north-south meander of the westerly jet affects the asymmetric structural change of the TC.

Data Availability Statement

The RSMC-Tokyo best track product is available at https://www.jma.go.jp/jma/jma-eng/jma-center/rsmc-hp-pub-eg/besttrack.html. The JTWC best track data is available at https://www.metoc.navy.mil/jtwc/jtwc.html?best-tracks. The JRA-55 reanalysis is available at https://jra.kishou.go.jp/JRA-55/index en.htm. The GSMaP data by JAXA is available at ftp.gportal.jaxa.jp. The datasets generated in this study are available from the corresponding author on reasonable request.

Supplement

Figure S1 presents annual frequency of all TCs, ET and the ratio of ET to all TCs from 2016 to 2020, and annual frequency of LA, SM and MID TCs.

Acknowledgements

We appreciate the editor and two anonymous reviewers for their careful peer review, important comments, and suggestions that improved this article. This study was supported by Japan Society for the Promotion of Science Grants-in-Aid for Scientific Research (KAKENHI) Grant Number JP19H01973, JP19H05696 and 22K03725.

References

Archambault, H. M., 2011: The downstream extratropical flow response to recurving western North Pacific tropical cyclones. Ph.D. dissertation, University at Albany, State University of New York, 212 pp.

Archambault, H. M., L. F. Bosart, D. Keyser, A. R. Aiyyer, and J. M. Cordeira, 2013: A climatological analysis of the extratropical flow response to recurving western North Pacific tropical cyclones. *Mon. Wea. Rev.*, **141**, 2325-2346.

Archambault, H. M., D. Keyser, L. F. Bosart, C. A. Davis, and J. M. Cordeira, 2015: A composite perspective of the extratropical flow response to recurving western North Pacific tropical cyclones. *Mon. Wea. Rev.*, **143**, 1122-1141.

Atallah, E. H., and L. F. Bosart, 2003: The extratropical transition and precipitation distribution of Hurricane Floyd (1999). *Mon. Wea. Rev.*, **131**, 1063-1081.

Evans, C., K. M. Wood, S. D. Aberson, H. M. Archambault, S. M. Milrad, L. F. Bosart, K. L. Corbosiero, C. A. Davis, J. R. Dias Pinto, J. Doyle, C. Fogarty, T. J. Galarneau, C. M. Grams, K. S. Griffin, J. Gyakum, R. E. Hart, N. Kitabatake, H. S. Lentink, R. McTaggart-Cowan, W. Perrie, J. F. Quinting, C. A. Reynolds, M. Riemer, E. A. Ritchie, Y. Sun, and F. Zhang, 2017: The extratropical transition of tropical cyclones. Part I: Cyclone evolution and direct impacts. *Mon. Wea. Rev.*, **145**, 4317-4344.

Evans, J. L., and R. E. Hart, 2003: Objective indicators of the life cycle evolution of extratropical transition for Atlantic tropical cyclones. *Mon. Wea. Rev.*, **131**, 909-925.

Evans, C., and R. E. Hart, 2008: Analysis of the wind field evolution associated with the extratropical transition of Bonnie (1998). *Mon. Wea. Rev.*, **136**, 2047-2065.

Finocchio, P. M., and J. D. Doyle, 2019: How the speed and latitude of the jet stream affect the downstream response to recurving tropical cyclones. *Mon. Wea. Rev.*, **147**, 3261-3281.

Grams, C. M., 2011: Quantification of the downstream impact of extratropical transition for Typhoon Jangmi and other case studies. Ph.D. dissertation, Karlsruhe Institute of Technology, 334 pp.

Grams, C. M. and H. M. Archambault, 2016: The key role of diabatic outflow in amplifying the midlatitude flow: A representative case study of weather systems surrounding Western North Pacific extratropical transition. *Mon. Wea. Rev.*, **144**, 3847-3869.

Grams, C. M., S. C. Jones, C. A. Davis, P. A. Harr, and M. Weissmann, 2013: The impact of Typhoon Jangmi (2008) on the midlatitude flow. Part I: Upper-level ridge building and modification of the jet. *Quart. J. Roy. Meteor. Soc.*, **139**, 2148-2164.

Hart, 2003: A cyclone phase space derived from thermal wind and thermal asymmetry. *Mon. Wea. Rev.*, **131**, 585-616.

Hoskins, B. J., M. E. McIntyre, and A. W. Robertson, 1985: On the use and significance of isentropic potential vorticity maps. *Quart. J. Roy. Meteor. Soc.*, **111**, 877-946.

Iizuka, S., R. Kawamura, H. Nakamura, and T. Miyama, 2021: Influence of warm SST in the Oyashio region on rainfall distribution of Typhoon Hagibis (2019). *SOLA*, **17A**, 21-28.

Ito, K., and H. Ichikawa, 2021: Warm ocean accelerating tropical cyclone Hagibis (2019) through interaction with a midlatitude westerly jet. *SOLA*, **17A**, 1-6.

Japan Meteorological Agency, 2019a: *A preliminary report on summary of weather and typhoons in 2019.* [Available at https://www.jma.go.jp/jma/press/1912/23a/press_2019matome.html.] (in Japanese).

Japan Meteorological Agency, 2019b: *A preliminary report on heavy rainfalls and strong winds by Typhoon Hagibis (2019).* [Available at http://www.data.jma.go.jp/obd/stats/data/bosai/report/2019/20191012/20191012.html.] (in Japanese).

Japan Meteorological Agency, 2020a: *A disaster report on heavy rains and strong winds by Typhoon Faxai (2019) and fronts from 13 August to 23 September.* [Available at https://www.jma.go.jp/jma/kishou/books/saigaiji/saigaiji_202002.pdf.] (in Japanese).

Japan Meteorological Agency, 2020b: *RSMC best track data.* [Available at https://www.jma.go.jp/jma/jma-eng/jma-center/rsmc-hp-pub-eg/besttrack.html.] (Accessed on 10 February 2021).

Joint Typhoon Warning Center, 2022: *JTWC best track data.* [Available at https://www.metoc.navy.mil/jtwc/jtwc.html?best-tracks.] (Accessed on 22 August 2022).

Jones, S. C., P. A. Harr, J. Abraham, L. F. Bosart, P. J. Bowyer, J. L. Evans, D. E. Hanley, B. N. Hanstram, R. E. Hart, F. Lalaurette, M. R. Sinclair, R. K. Smith, and C. Thorncroft, 2003: The extratropical transition of tropical cyclones: Forecast challenges, current understanding, and future directions. *Wea. Forecasting*, **18**, 1052-1092.

Kawase, H., M. Yamaguchi, Y. Imada, S. Hayashi, A. Murata, T. Nakaegawa, T. Miyasaka, and I. Takayabu, 2021: Enhancement of extremely heavy precipitation induced by Typhoon Hagibis (2019) due to historical warming. *SOLA*, **17A**, 7-13.

Keller, J. H., C. M. Grams, M. Riemer, H. M. Archambault, L. Bosart, J. D. Doyle, J. L. Evans, T. J. Galarneau, K. Griffin, P. A. Harr, N. Kitabatake, R. McTaggart-Cowan, F. Pantillon, J. F. Quinting, C. A. Reynolds, E. A. Ritchie, R. D. Torn, and F. Zhang, 2019: The extratropical transition of tropical cyclones. Part II: Interaction with the midlatitude flow, downstream impacts, and implications for predictability. *Mon. Wea. Rev.*, **147**, 1077-1106.

Kitabatake, N., 2011: Climatology of extratropical transition of tropical cyclones in the western North Pacific defined by using cyclone phase space. *J. Meteor. Soc. Japan*, **89**, 309-325.

Kitabatake, N., 2019: *Synoptic Meteorology foundation edition*, Japan Meteorological Agency Press, 341 pp (in Japanese). [Available at https://www.jma.go.jp/jma/kishou/know/expert/pdf/textbook_synop_basic_20210831.pdf.]

Kobayashi, S., Y. Ota, Y. Harada, A. Ebita, M. Moriya, H. Onoda, K. Onogi, H. Kamahori, C. Kobayashi, H. Endo, K. Miyaoka, and K. Takahashi, 2015: The JRA-55 Reanalysis: General specifications and basic characteristics. *J. Meteor. Soc. Japan*, **93**, 5-48.

Kubota, T., K. Aonashi, T. Ushio, S. Shige, Y. N. Takayabu, M. Kachi, Y. Arai, T. Tashima, T. Masaki, N. Kawamoto, T. Mega, M. K. Yamamoto, A. Hamada, M. Yamaji, G. Liu and R. Oki 2020: Global Satellite Mapping of Precipitation (GSMaP) products in the GPM era. *Satellite precipitation measurement*, Springer, doi:10.1007/978-3-030-24568-9_20.

Miyamoto, Y., H., Fudeyasu, and A., Wada, 2022: Intensity and Structural Changes of Numerically Simulated Typhoon Faxai (1915) before Landfall. *J. Meteor. Soc.*, **100**, 181-196.

Quinting, J. F., and S. C. Jones, 2016: On the impact of tropical cyclones on Rossby wave packets: A climatological perspective. *Mon. Wea. Rev.*, **144**, 2021-2048.

Riboldi, C. M. Grams, M. Riemer, and H. M. Archambault, 2019: A phase locking perspective on Rossby wave amplification and atmospheric blocking downstream of recurving western North Pacific tropical cyclones. *Mon. Wea. Rev.*, **147**, 567-589.

Riboldi, J., M. Röthlisberger, and C. M. Grams, 2018: Rossby wave initiation by recurving tropical cyclones in the western North Pacific. *Mon. Wea. Rev.*, **146**, 1283-1301.

Shin, J.H., 2019: Vortex spinup process in the extratropical transition of Hurricane Sandy (2012). *J. Atmos. Sci.*, **76**, 3589-3610.

Takamura, N., A. Wada, 2020: Unusual Characteristics of Extratropical Transition of Typhoons in August 2016. *J. Meteor. Soc. Japan,* **98**, 691-706.

Takemi, T. and T. Unuma, 2020: Environmental Factors for Heavy Rainfall during Typhoon Hagibis (2019). *SOLA*, **16**, 30-36.

Yanase, W., K. Araki, A. Wada, U. Shimada, M. Hayashi and T. Horinouchi, 2022: Multiple dynamics of precipitation concentrated on the north side of typhoon Hagibis (2019) during extratropical transition. *J. Meteor. Soc. Japan*, **100**, 783-805.

Wada, A., and J. C. L. Chan, 2021: Increasing TCHP in the western North Pacific and its influence on the intensity of FAXAI and HAGIBIS in 2019. *SOLA*, **17A**, 29-32.

List of Figures

Fig. 1 Tracks of TCs from 2016 to 2020: (a) LA-ETR TCs (red solid lines), and (b) SM-ETR (blue solid lines) and SM-SCS TCs (blue dashed lines) defined in Section 2.2. Circles, triangles and squares indicate positions at TM, TB and TE, respectively. Closed red (blue) symbols indicate the mean positions for LA-ETR (SM-ETR) TCs. Identifiers such as “T1915” and “T1919” indicate the individual TCs. Star symbol in (b) indicates the location of Tokyo.

Fig. 2 Time series of CPS parameters (a) $-V_T^L$, (b) $-V_T^U$, (c) B (m), and (d) number of data samples from 36 hours before TB (TB − 36) to 36 hours after TE (TE + 36). Red (blue) lines indicate the values composited for LA-ETR (SM-ETR) TCs defined in Section 2.2 on the basis of time relative to TB and TE. The data from TB to TE is composited on the basis of time relative to TB, and the number of data samples differs because this duration for an individual TC is different. The data is plotted only when there are three or more TCs at a time slot. The error bars represent the standard deviations. Red (blue) dashed lines indicate the results for T1919 (T1915). Black lines indicate the criterion ($-V_T^L$ and -

$V_T^U = 0$, $B = 10$ m).

Fig. 3 Scatter diagram of Max_R25 (horizontal axis, nm) and Max_R15 (vertical axis, nm) for all TCs (ET + no-ET) from 2016 to 2020. Black dashed lines indicate the criterion (Max_R25 = 120 nm and 70 nm, Max_R15 = 350 nm and 200 nm). Red, blue and green circles (triangles) indicate LA, SM and MID TCs for ET (no-ET) cases, respectively. Red and blue frames show LA and SM types, respectively.

Fig. 4 (a) Percentages of the number of LA (red), SM (blue) and MID (green) TCs among all TCs from 2016 to 2020. (b) is the same as (a), but for among ET cases.

Fig. 5 (a) Monthly frequency of all TCs and ET (blue and red bars, left axis), and the ratio of ET to all TCs (green line, right axis, %) from 2016 to 2020. (b) is the same as (a), but for frequency of LA, SM and MID TCs (red, blue and green bars), and the ratio of LA and SM TCs to all TCs (red and blue lines).

Fig. 6 Composited horizontal distributions of temperature at 850 hPa around the TC center at (a) TB and (b) TE for LA-ETR TCs. The contour interval is 2 K. (c) and (d) are the same as (a) and (b), but for SM-ETR TCs. The location of TC center is indicated by the blue circle. Vertical and horizontal axes indicate the distance from the TC center in degree.

Fig. 7 Same as Fig. 6, but for horizontal wind (color) and geopotential height (contour with an interval of 50 m) at 300 hPa.

Fig. 8 Horizontal distributions of (a) 355-K isentropic PV, and (b) 300-hPa horizontal wind (color) and geopotential height (contour) at 00 UTC on 12 October, corresponding to TB for T1919. The location of TC center is indicated by the white circle in (a) and (c), and the black circle in (b) and (d). The contour intervals for PV and geopotential height are 1 PVU and 50 m, respectively. (c) and (d) are the same as (a) and (b), but for 06 UTC on 13 October, corresponding to TE for T1919.

Fig. 9 Same as Fig. 8, but (a) and (b) at 06 UTC on 09 September, and (c) and (d) at 12 UTC on 09 September, which are corresponding to TB and TE for T1915.

Fig. 10 Horizontal distributions of 24-hour accumulated precipitation (color) at (a) 00 UTC on 12 October and (b) 06 UTC on 13 October, corresponding to TB and TE for T1919, and (c) 06 UTC on 09 September and (d) 12 UTC on 09 September, corresponding to TB and TE for T1915. The location of TC center is indicated by the black circle with the origin of black arrow showing the location 24 hours before.

Fig. 11 Time series of PWAT (line, left axis, $*10^{13}$ kg) from 36 hours before TB (TB − 36) to 36 hours after TE (TE + 36). The values are area-integrated within Max_R15 for each TC. Red (blue) lines indicate the values composited for LA-ETR (SM-ETR) TCs on the basis of time relative to TB and TE. Red (blue) bars represent the number of data samples for LA-ETR (SM-ETR) TCs (right axis). The data from TB to TE is composited on the basis of time relative to TB, and the number of data samples differs because this duration for an individual TC is different. The data is plotted only when there are three or more TCs at a time slot.

Fig. 12 Minimum central pressure (horizontal axis, hPa) and maximum sustained wind speed (vertical axis, m s^{-1}) during the life cycle of the individual TC. Red (blue) circles indicate LA-ETR (SM-ETR) TCs.

Fig. 13 RMW at TM (horizontal axis, km) and that at TE (vertical axis, km) of each TC. Red (blue) circles indicate LA-ETR (SM-ETR) TCs. Black dashed line shows when the RMW at TM equals that at TE.

Fig. 14 Schematic diagram on the interactions of TCs with a westerly jet with a focus on the differences between LA-ETR and SM-ETR TCs. The LA-ETR TCs drastically change into asymmetric structures while they move northward along the westerly jet with increasing the amplitude of the north-south meander. The LA-ETR TCs interact with the westerly jet, whereas such interactions rarely occur for the SM-ETR TCs.

List of Tables

Table 1 LA-ETR, SM-ETR and SM-SCS TCs defined in Section 2.2. TC name is listed in column 2; TC number in column 3; ET time (UTC) based on the CPS analysis (TB: B > 10 m and TE: $-V_T^L < 0$) in column 4 and 5; Max_R25 (nm / km) and Max_R15 (nm / km) in column 6 and 7.

Table 2 Mean and standard deviation (in parenthesis) for characteristics of LA-ETR and SM-ETR TCs. Bold italic indicates the difference between LA-ETR and SM-ETR TCs is significant at the 95% significance level based on the two-sided Student's *t*-test.

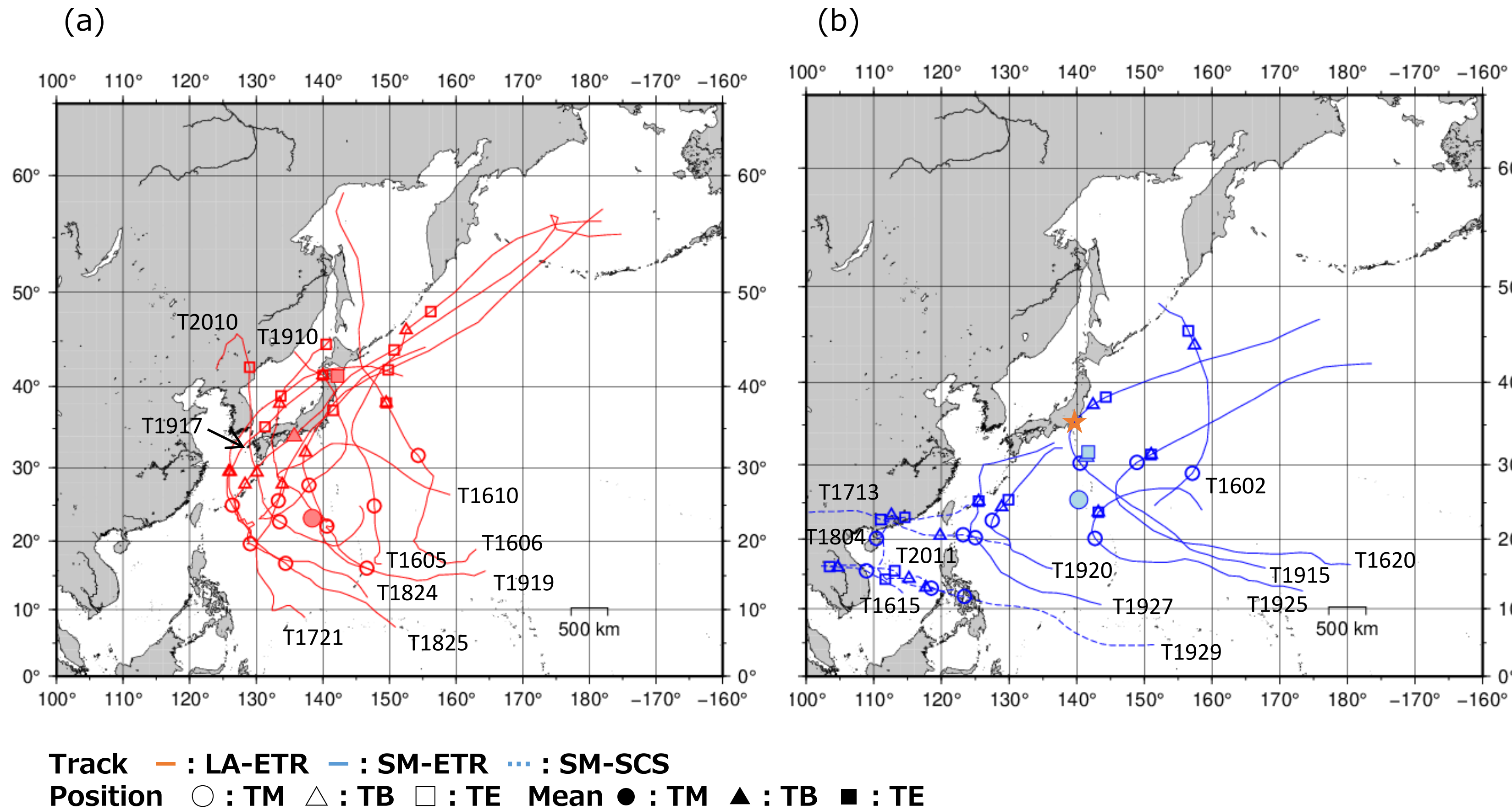

Fig. 1 Tracks of TCs from 2016 to 2020: (a) LA-ETR TCs (red solid lines), and (b) SM-ETR (blue solid lines) and SM-SCS TCs (blue dashed lines) defined in Section 2.2. Circles, triangles and squares indicate positions at TM, TB and TE, respectively. Closed red (blue) symbols indicate the mean positions for LA-ETR (SM-ETR) TCs. Identifiers such as “T1915” and “T1919” indicate the individual TCs. Star symbol in (b) indicates the location of Tokyo.

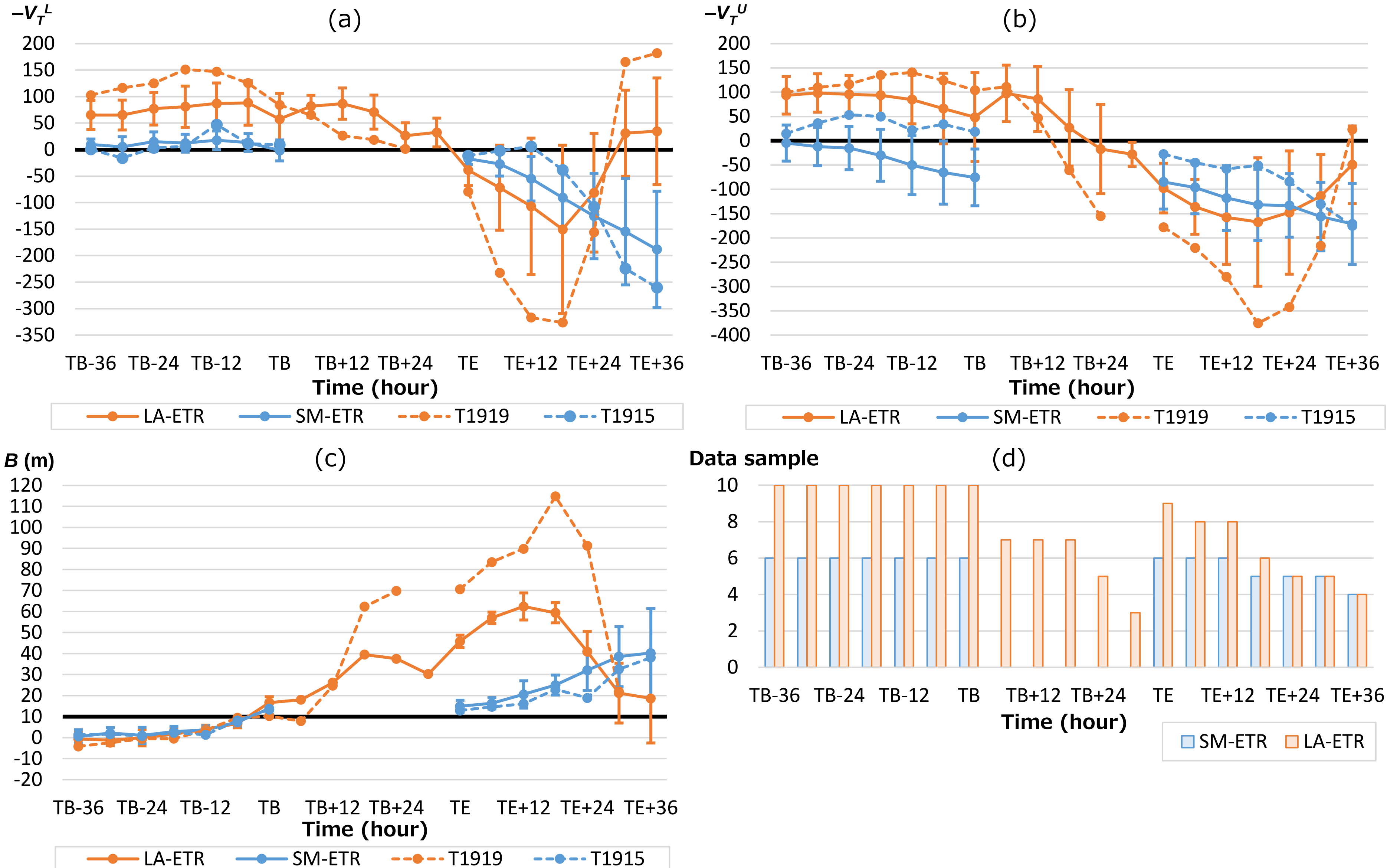

Fig. 2 Time series of CPS parameters (a) $-V_T^L$, (b) $-V_T^U$, (c) B (m), and (d) number of data samples from 36 hours before TB (TB − 36) to 36 hours after TE (TE + 36). Red (blue) lines indicate the values composited for LA-ETR (SM-ETR) TCs defined in Section 2.2 on the basis of time relative to TB and TE. The data from TB to TE is composited on the basis of time relative to TB, and the number of data samples differs because this duration for an individual TC is different. The data is plotted only when there are three or more TCs at a time slot. The error bars represent the standard deviations. Red (blue) dashed lines indicate the results for T1919 (T1915). Black lines indicate the criterion ($-V_T^L$ and $-V_T^U = 0$, $B = 10$ m).

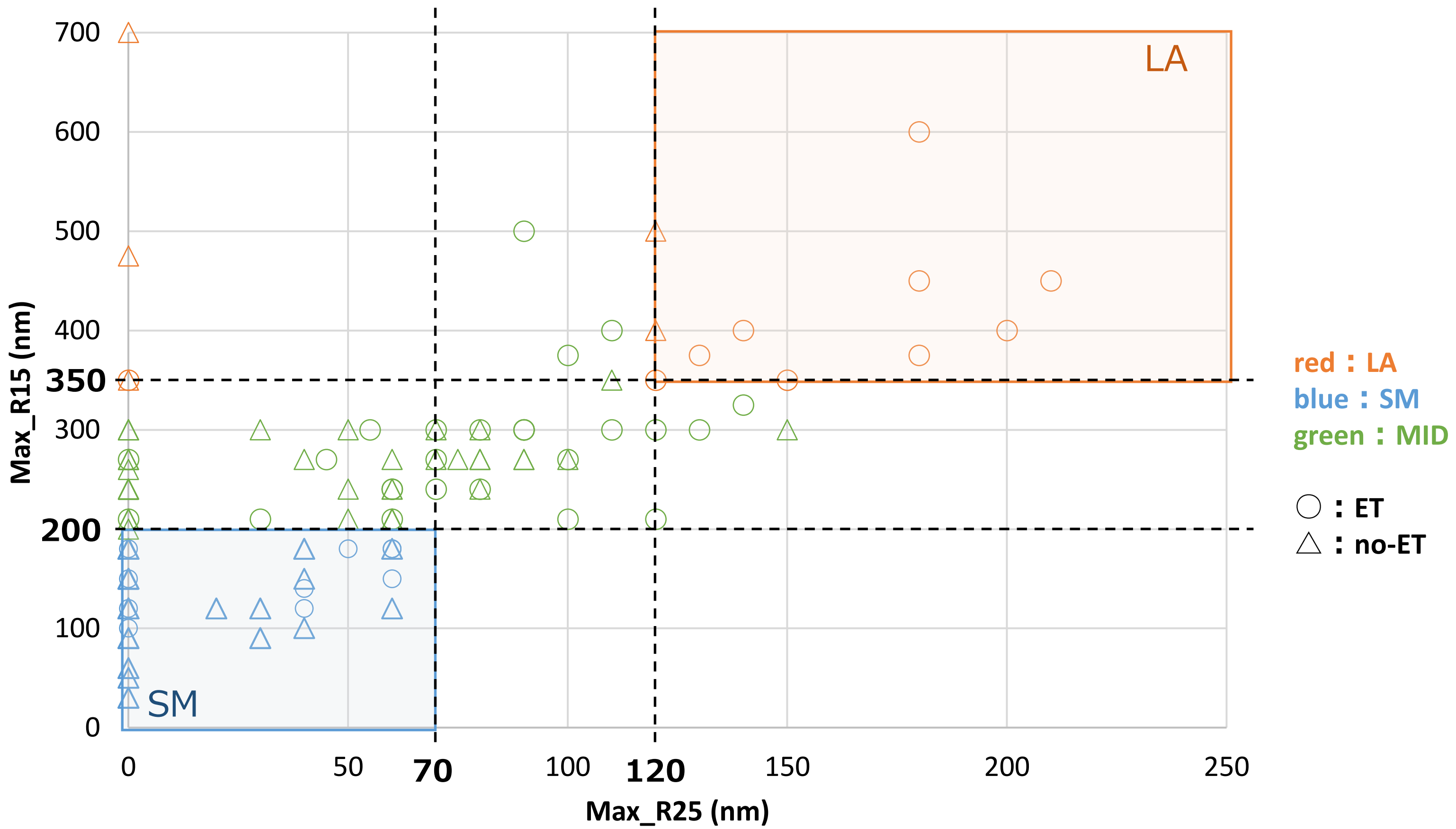

Fig. 3 Scatter diagram of Max_R25 (horizontal axis, nm) and Max_R15 (vertical axis, nm) for all TCs (ET + no-ET) from 2016 to 2020. Black dashed lines indicate the criterion (Max_R25 = 120 nm and 70 nm, Max_R15 = 350 nm and 200 nm). Red, blue and green circles (triangles) indicate LA, SM and MID TCs for ET (no-ET) cases, respectively. Red and blue frames show LA and SM types, respectively.

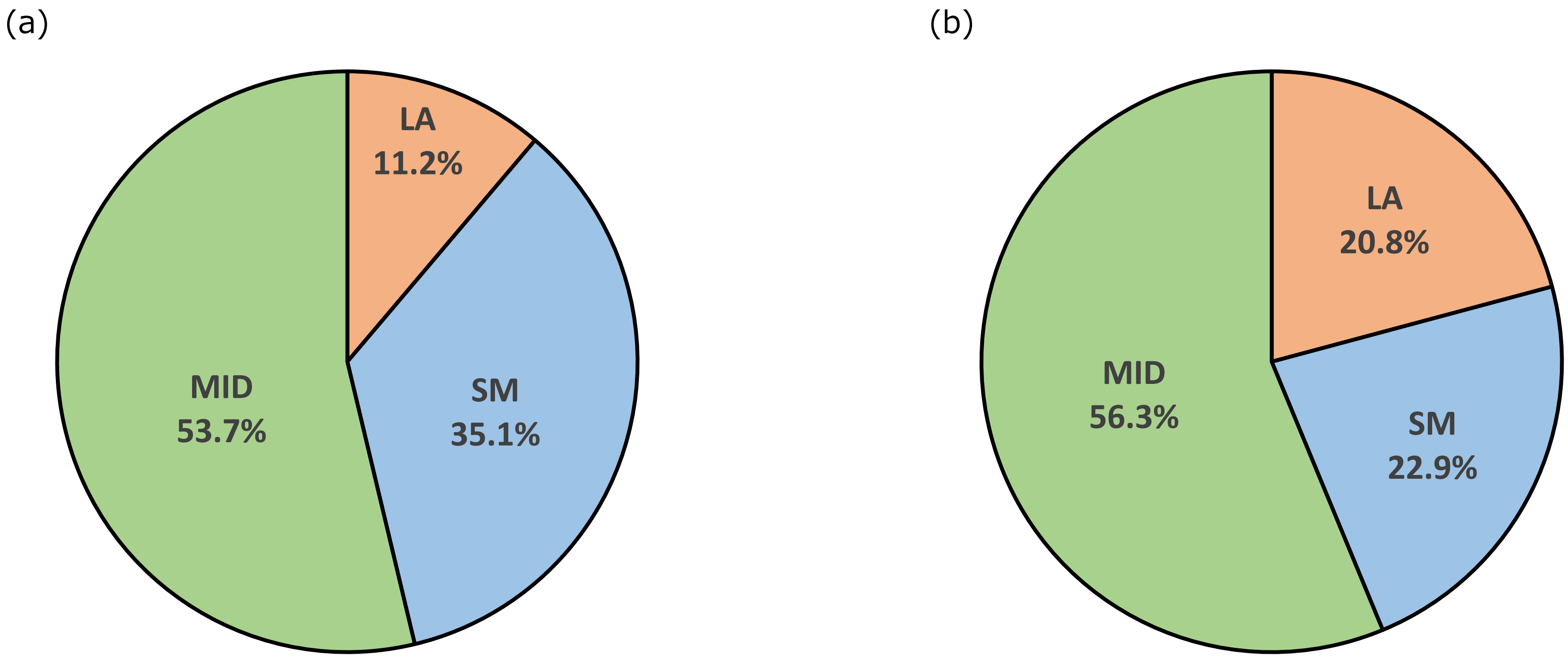

Fig. 4 (a) Percentages of the number of LA (red), SM (blue) and MID (green) TCs among all TCs from 2016 to 2020. (b) is the same as (a), but for among ET cases.

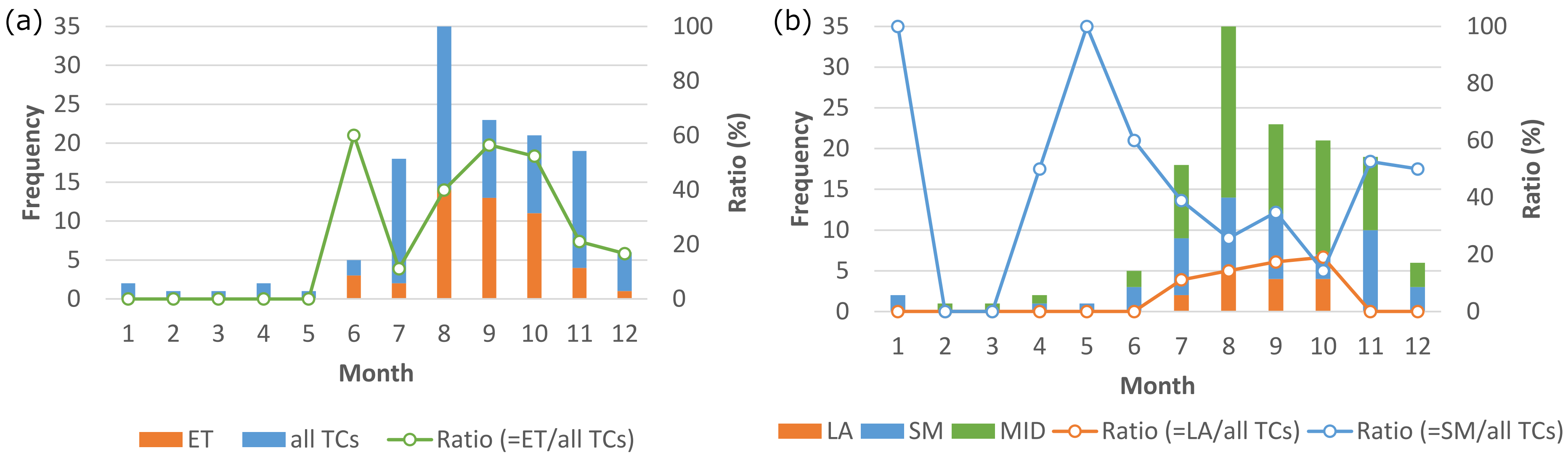

Fig. 5 (a) Monthly frequency of all TCs and ET (blue and red bars, left axis), and the ratio of ET to all TCs (green line, right axis,%) from 2016 to 2020. (b) is the same as (a), but for frequency of LA, SM and MID TCs (red, blue and green bars), and the ratio of LA and SM TCs to all TCs (red and blue lines).

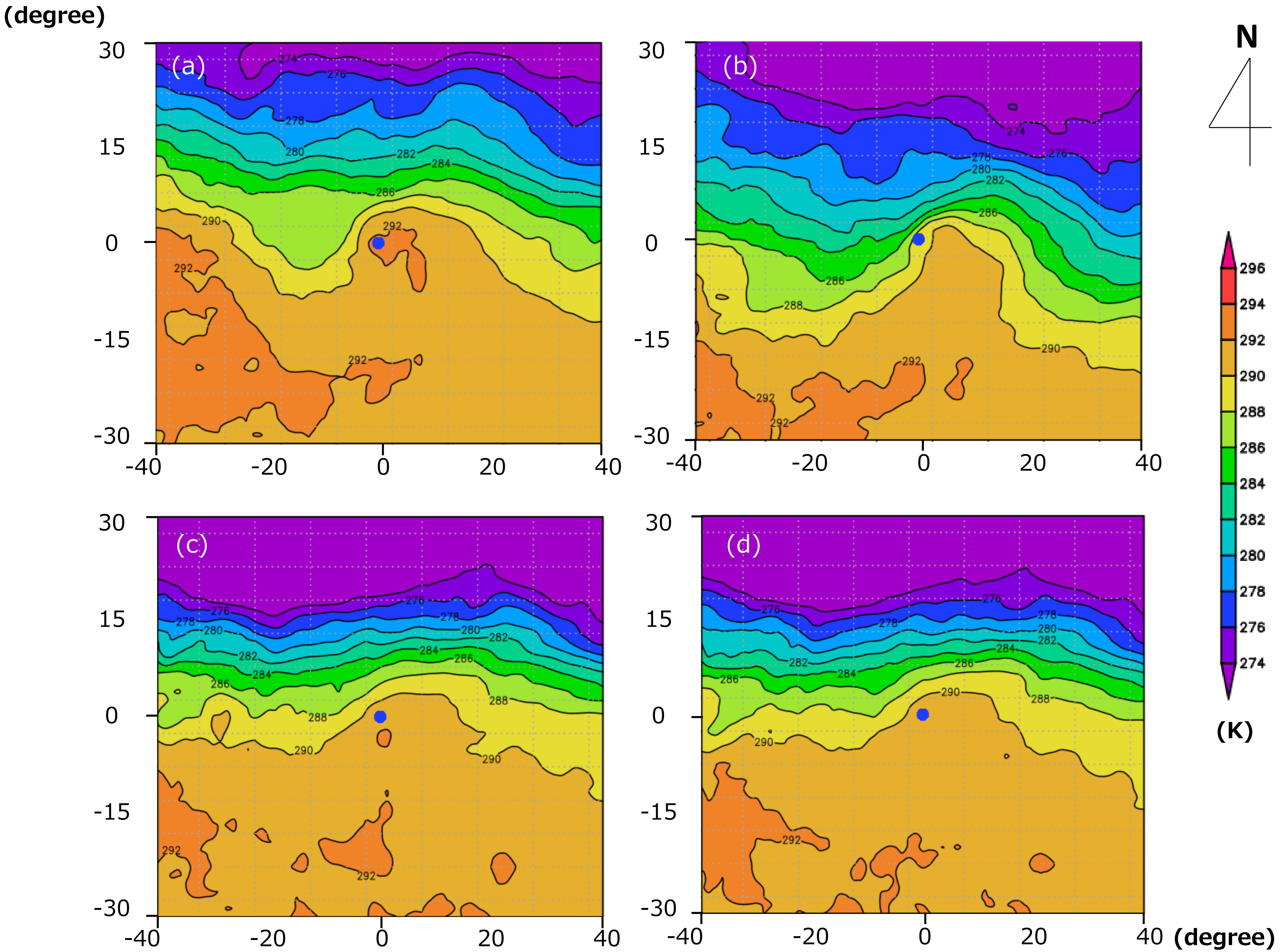

Fig. 6 Composited horizontal distributions of temperature at 850 hPa around the TC center at (a) TB and (b) TE for LA-ETR TCs. The contour interval is 2 K. (c) and (d) are the same as (a) and (b), but for SM-ETR TCs. The location of TC center is indicated by the blue circle. Vertical and horizontal axes indicate the distance from the TC center in degree.

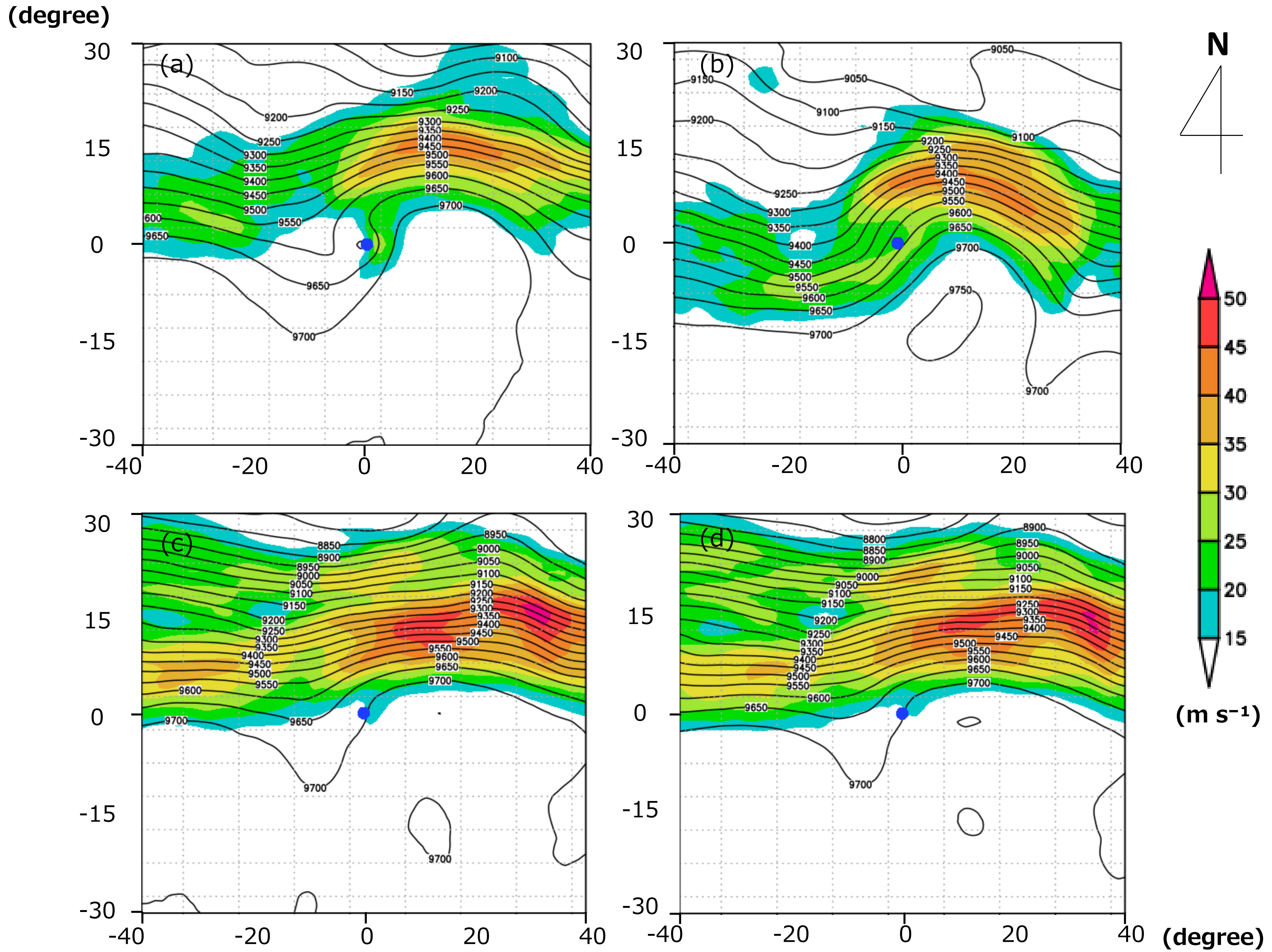

Fig. 7 Same as Fig. 6, but for horizontal wind (color) and geopotential height (contour with an interval of 50 m) at 300 hPa.

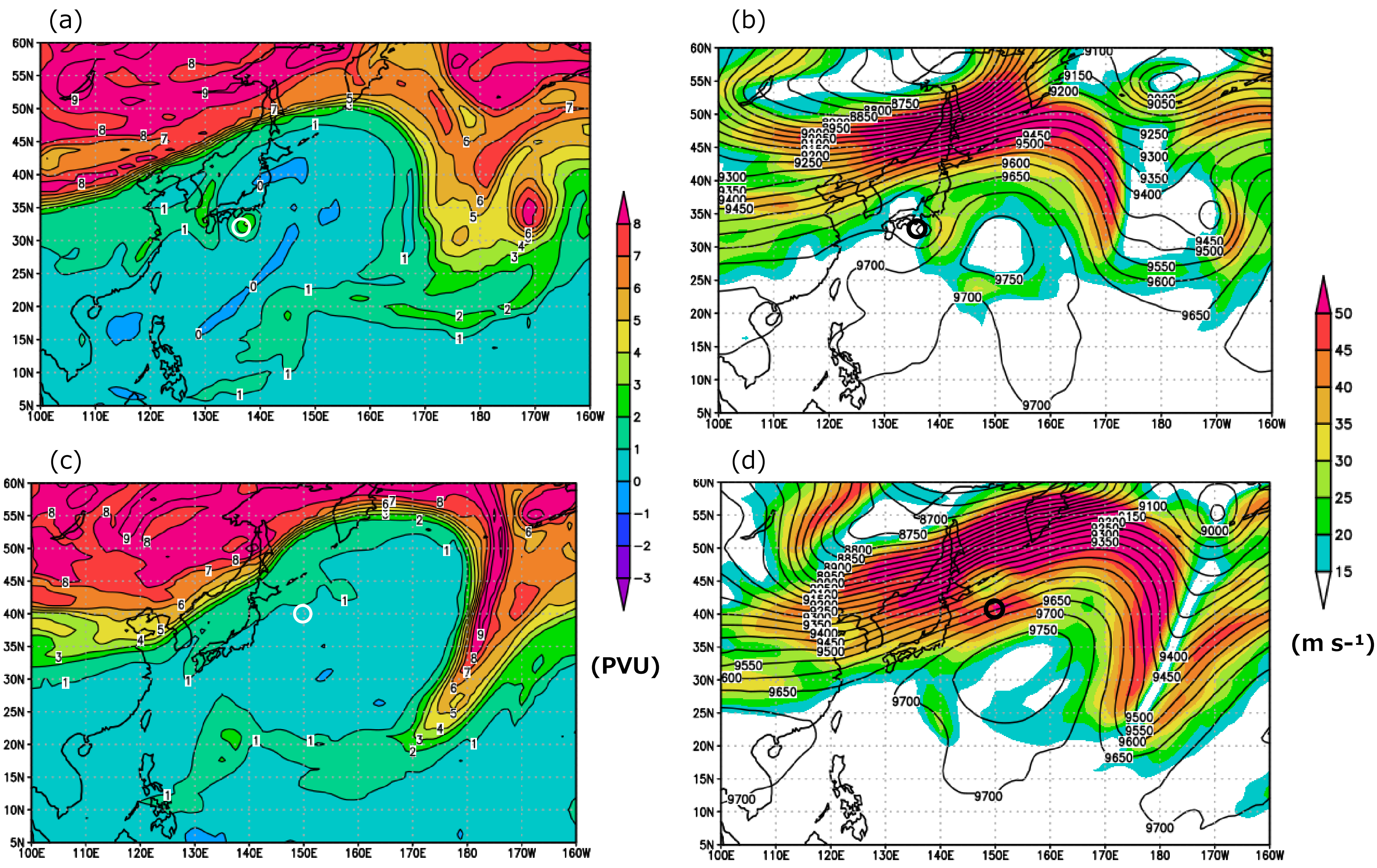

Fig. 8 Horizontal distributions of (a) 355-K isentropic PV, and (b) 300-hPa horizontal wind (color) and geopotential height (contour) at 00 UTC on 12 October, corresponding to TB for T1919. The location of TC center is indicated by the white circle in (a) and (c), and the black circle in (b) and (d). The contour intervals for PV and geopotential height are 1 PVU and 50 m, respectively. (c) and (d) are the same as (a) and (b), but for 06 UTC on 13 October, corresponding to TE for T1919.

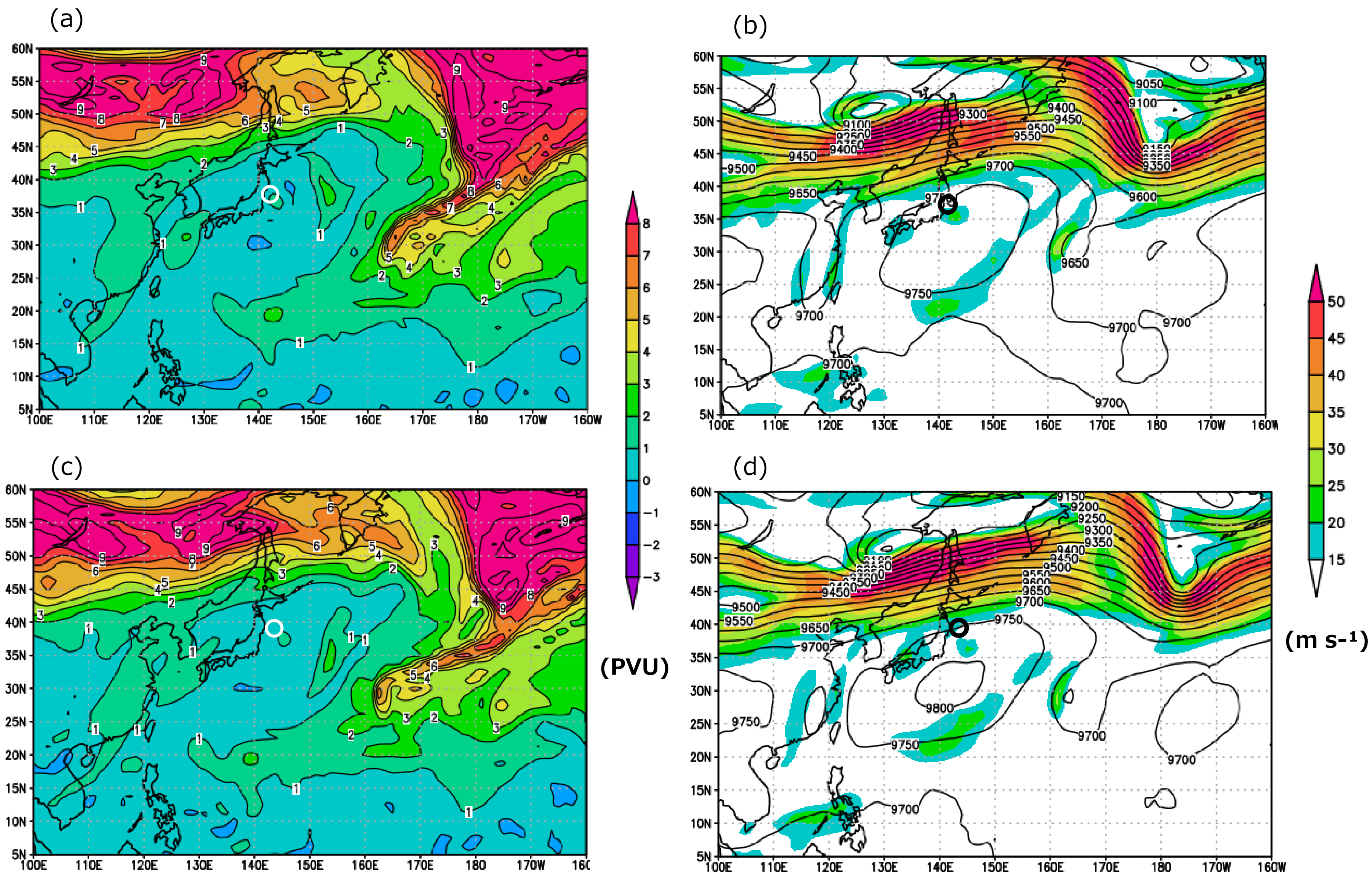

Fig. 9 Same as Fig. 8, but (a) and (b) at 06 UTC on 09 September, and (c) and (d) at 12 UTC on 09 September, which are corresponding to TB and TE for T1915.

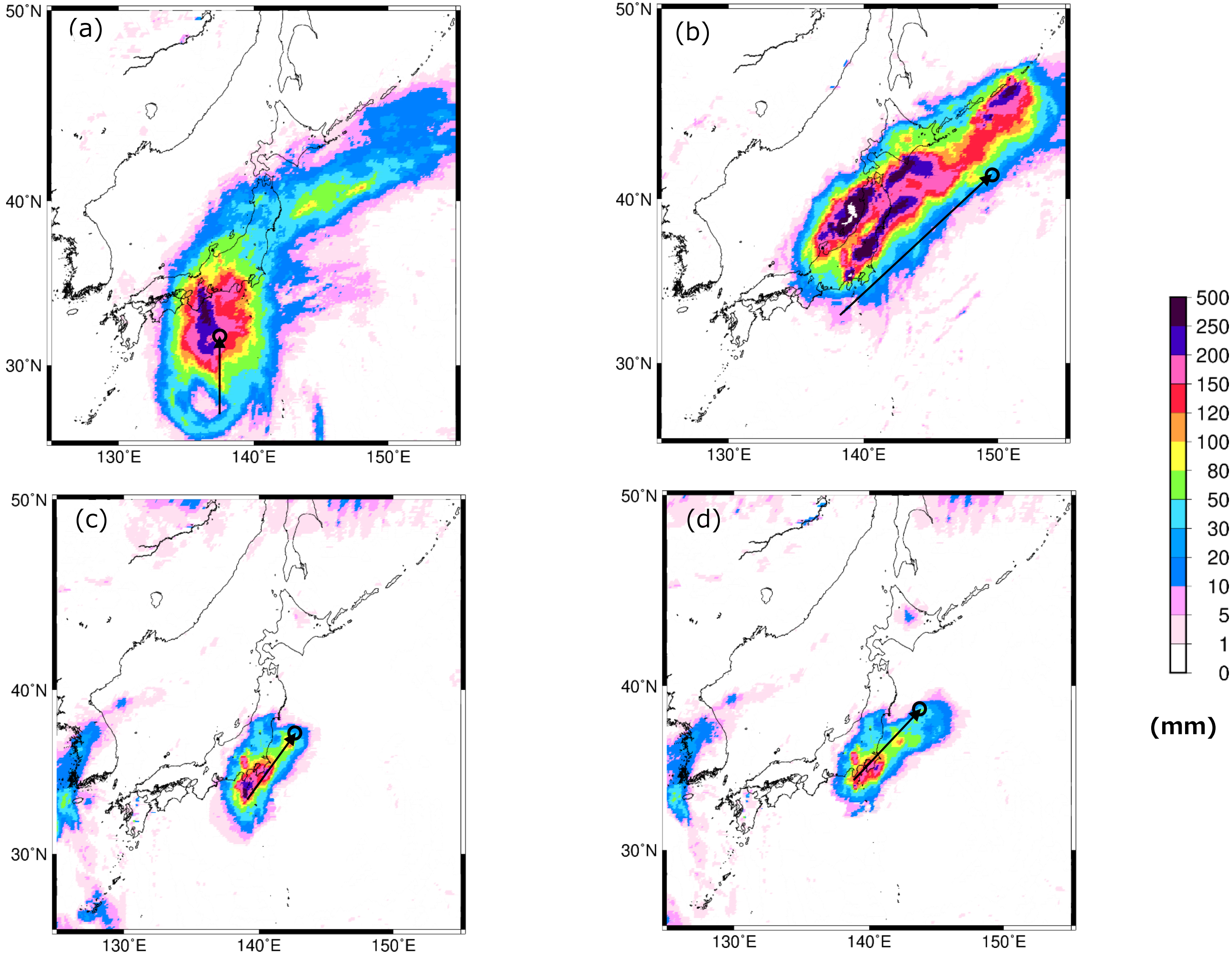

Fig. 10 Horizontal distributions of 24-hour accumulated precipitation (color) at (a) 00 UTC on 12 October and (b) 06 UTC on 13 October, corresponding to TB and TE for T1919, and (c) 06 UTC on 09 September and (d) 12 UTC on 09 September, corresponding to TB and TE for T1915. The location of TC center is indicated by the black circle with the origin of black arrow showing the location 24 hours before.

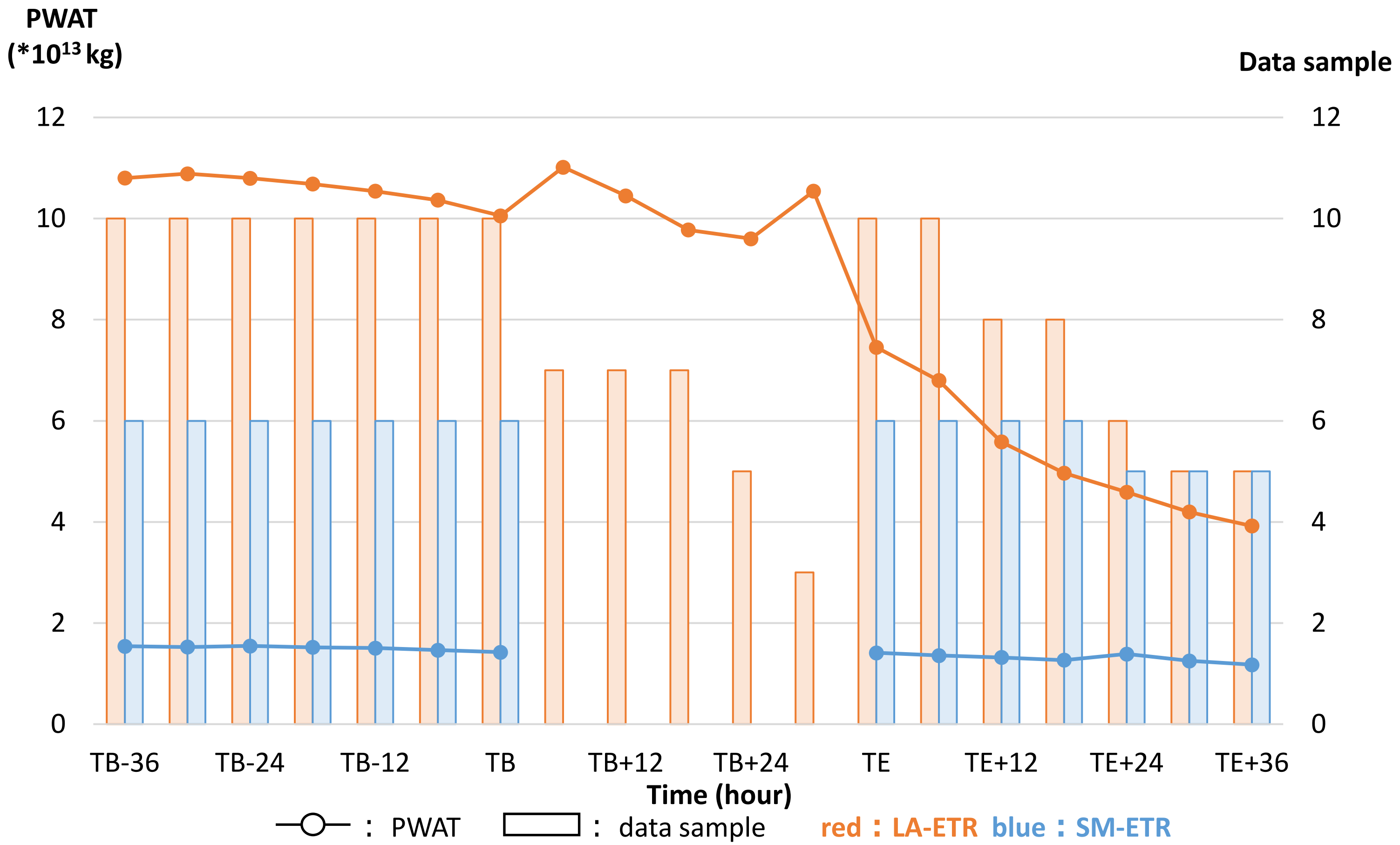

Fig. 11 Time series of PWAT (line, left axis, $*10^{13}$ kg) from 36 hours before TB (TB − 36) to 36 hours after TE (TE + 36). The values are area-integrated within Max_R15 for each TC. Red (blue) line indicate the values composited for LA-ETR (SM-ETR) TCs on the basis of time relative to TB and TE. Red (blue) bars represent the number of data samples for LA-ETR (SM-ETR) TCs (right axis). The data from TB to TE is composited on the basis of time relative to TB, and the number of data samples differs because this duration for an individual TC is different. The data is plotted only when there are three or more TCs at a time slot.

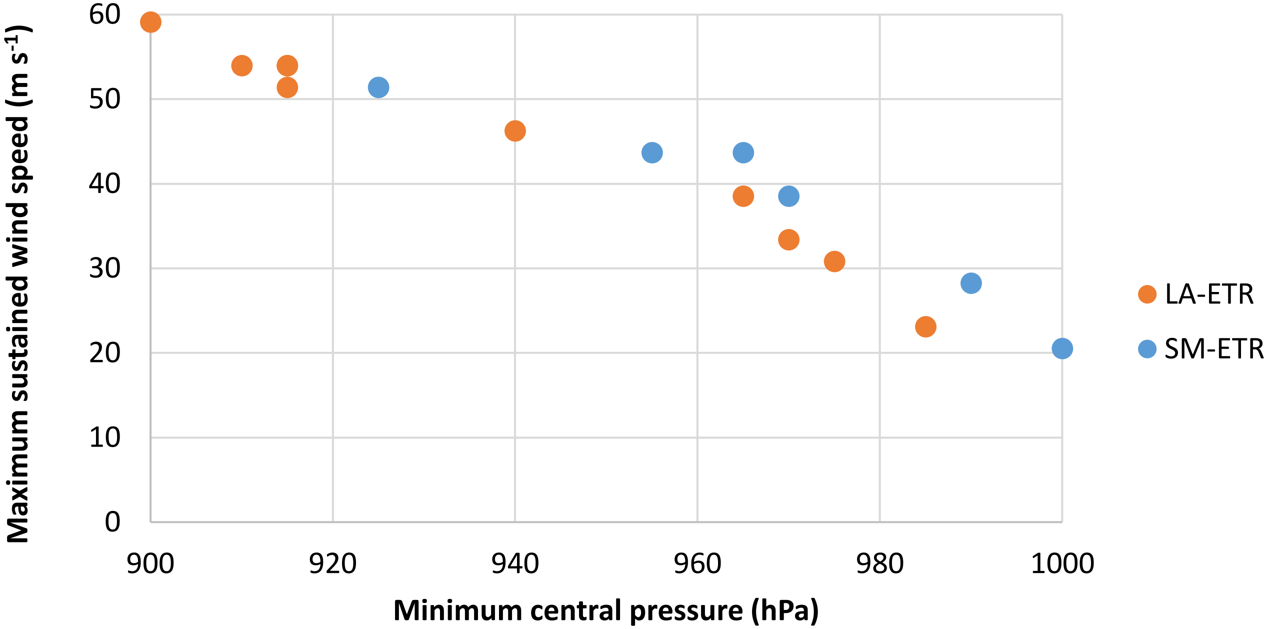

Fig. 12 Minimum central pressure (horizontal axis, hPa) and maximum sustained wind speed (vertical axis, m s^{-1}) during the life cycle of the individual TC. Red (blue) circles indicate LA-ETR (SM-ETR) TCs.

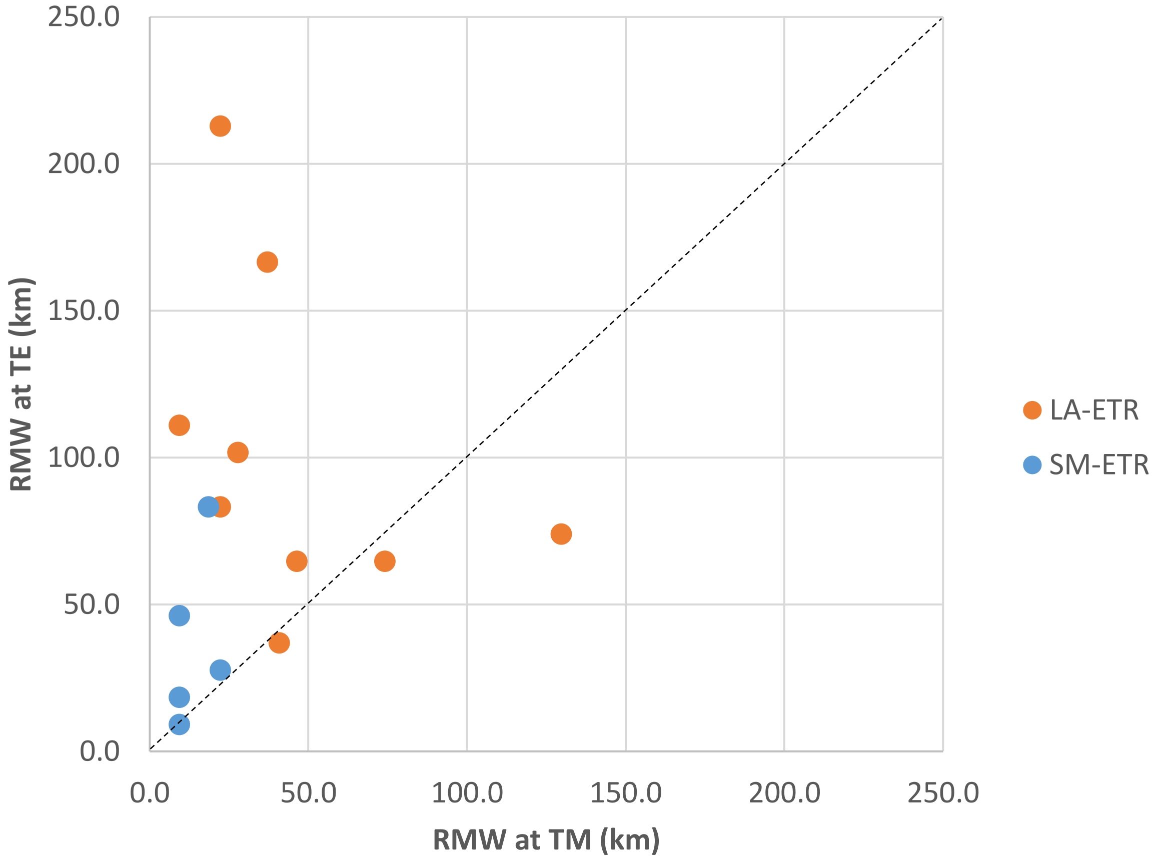

Fig. 13 RMW at TM (horizontal axis, km) and that at TE (vertical axis, km) for each TC. Red (blue) circles indicate LA-ETR (SM-ETR) TCs. Black dashed line shows when the RMW at TM equals that at TE.

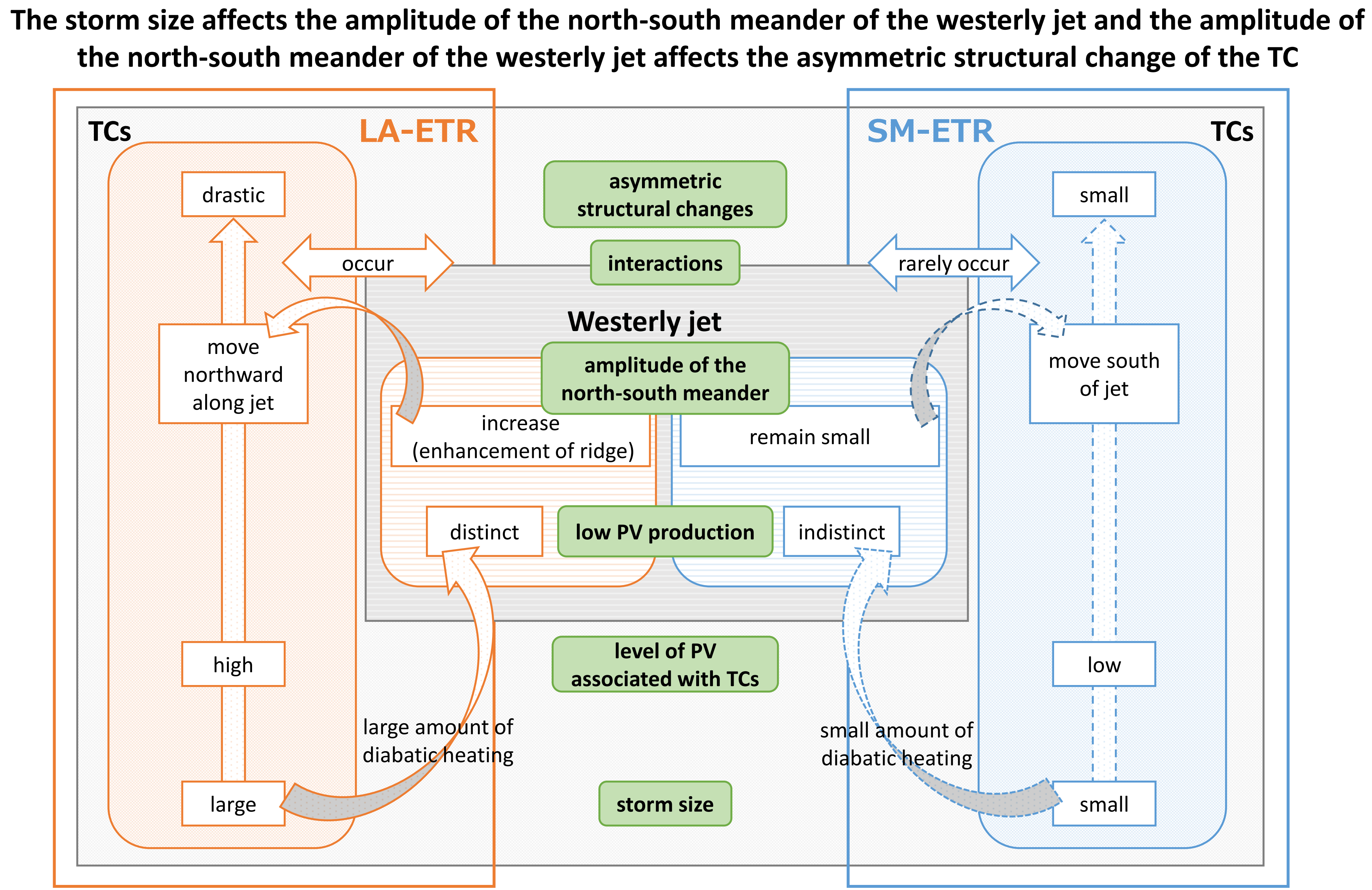

Fig. 14 Schematic diagram on the interactions of TCs with a westerly jet with a focus on the differences between LA-ETR and SM-ETR TCs. The LA-ETR TCs drastically change into asymmetric structures while they move northward along the westerly jet with increasing the amplitude of the north-south meander. The LA-ETR TCs interact with the westerly jet, whereas such interactions rarely occur for the SM-ETR TCs.

Table 1 LA-ETR, SM-ETR and SM-SCS TCs defined in Section 2.2. TC name is listed in column 2; TC number in column 3; ET time (UTC) based on the CPS analysis (TB: B > 10 m and TE: $-V_T^L < 0$) in column 4 and 5; Max_R25 (nm / km) and Max_R15 (nm / km) in column 6 and 7.

type	TC name	TC number	ET time (UTC)		Max_R25 (nm / km)	Max_R15 (nm / km)
			TB (B > 10 m)	TE ($-V_T^L < 0$)		
LA-ETR	OMAIS	T1605	00UTC 10 Aug	06UTC 10 Aug	180 / 333.4	375 / 694.5
	CONSON	T1606	06UTC 14 Aug	06UTC 14 Aug	0 / 0	350 / 648.2
	LIONROCK	T1610	12UTC 30 Aug	12UTC 30 Aug	120 / 222.2	350/ 648.2
	LAN	T1721	00UTC 22 Oct	00UTC 23 Oct	210 / 388.9	450 / 833.4
	TRAMI	T1824	12UTC 29 Sep	06UTC 1 Oct	150 / 277.8	350/ 648.2
	KONG-REY	T1825	06UTC 5 Oct	12UTC 6 Oct	140 / 259.3	400 / 740.8
	KROSA	T1910	18UTC 15 Aug	06UTC 17 Aug	180/ 333.4	600 / 1111.2
	TAPAH	T1917	18UTC 21 Sep	18UTC 22 Sep	130 / 240.8	375 / 694.5
	HAGIBIS	T1919	00UTC 12 Oct	06UTC 13 Oct	200 / 370.4	400 / 740.8
	HAISHEN	T2010	06UTC 6 Sep	18UTC 7 Sep	180/ 333.4	450 / 833.4
SM-ETR	LUPIT	T1602	06UTC 25 Jul	12UTC 25 Jul	0 / 0	100 / 185.2
	SONGDA	T1620	00UTC 12 Oct	00UTC 12 Oct	60 / 111.1	180 / 333.4
	FAXAI	T1915	06UTC 9 Sep	12UTC 9 Sep	60/ 111.1	180 / 333.4
	NEOGURI	T1920	06UTC 20 Oct	12UTC 20 Oct	40 / 74.1	140 / 259.3
	FENGSHEN	T1925	00UTC 16 Nov	00UTC 16 Nov	60/ 111.1	150 / 277.8
	FUNG-WONG	T1927	00UTC 23 Nov	00UTC 23 Nov	60/ 111.1	180 / 333.4
SM-SCS	RAI	T1615	12UTC 13 Sep	18UTC 13 Sep	0 / 0	150 / 277.8
	HATO	T1713	00UTC 22 Aug	12UTC 23 Aug	50 / 92.6	180 / 333.4
	EWINIAR	T1804	12UTC 8 Jun	12UTC 9 Jun	0 / 0	120 / 222.2
	PHANFONE	T1929	00UTC 28 Dec	00UTC 29 Dec	40 / 74.1	120 / 222.2
	NOUL	T2011	00UTC 16 Sep	06UTC 17 Sep	0 / 0	180 / 333.4

Table 2 Mean and standard deviation (in parenthesis) for characteristics of LA-ETR and SM-ETR TCs. Bold italic indicates the difference between LA-ETR and SM-ETR TCs is significant at the 95% significance level based on the two-sided Student's *t*-test.

		LA-ETR	SM-ETR
Mean Max_R15 (nm / km)		***410 (72.6) / 759.3 (134.5)***	***155 (17.4) / 287.1 (32.3)***
Mean latitude (degree)	TM	23.2 (4.6)	25.4 (4.5)
	TB	34.0 (6.1)	31.0 (7.6)
	TE	***41.2 (3.7)***	***31.6 (8.0)***
Mean duration (hour)	from TM to TB	***73.2 (50.5)***	***26.0 (15.0)***
	from TB to TE	***22.8 (14.6)***	***3.0 (3.0)***
Mean V_{move} ($m\ s^{-1}$)	before TB	6.2 (2.6)	6.2 (2.9)
	after TB	***9.3 (3.1)***	***5.4 (2.4)***
Mean U_{move} ($m\ s^{-1}$)	before TB	***-1.2 (2.4)***	***2.4 (3.2)***
	after TB	6.1 (11.2)	9.2 (9.5)
Mean minimum central pressure (hPa)		***939.0 (30.2)***	***967.5 (24.3)***
Mean maximum sustained wind speed ($m\ s^{-1}$)		44.5 (11.6)	37.7 (10.4)
Mean RMW (km)	TM	55.7 (44.9)	20.7 (16.4)
	TB	72.8 (58.9)	33.3 (25.9)
	TE	***101.9 (52.4)***	***37.0 (26.2)***